SUPPORTING INFORMATION

Triclinic metamaterials by tristable origami with reprogrammable frustration

Ke Liu,[1] Phanisri P. Pratapa,[2] Diego Misseroni,[3]
Tomohiro Tachi,[4] and Glaucio H. Paulino[5,*]

[1]*Department of Advanced Manufacturing and Robotics, Peking University, Beijing 100871, China*

[2]*Department of Civil Engineering, Indian Institute of Technology Madras, Chennai 600036, TN, India*

[3]*Department of Civil, Environmental and Mechanical Engineering, University of Trento, Trento 38123, Italy*

[4]*Graduate School of Arts and Sciences, University of Tokyo, Tokyo 153-8902, Japan*

[5]*Department of Civil and Environmental Engineering, Princeton Institute for the Science and Technology of Materials, Princeton University, Princeton, New Jersey, 08544, USA*

Contents

* gp1863@princeton.edu

I: Trimorph Geometry

The unit cell of the Trimorph pattern comprises a degree-4 vertex (denoted by O_5 in Fig. S1(a)) formed by the intersection of parallelogram shaped panels with edge lengths a and angles $\alpha+\delta$, α or $\alpha-\delta$, for $0<\alpha\leq 90°$, $0\leq\delta<\alpha$. The sum of opposite panel angles is equal to 2α and therefore, the Trimorph vertex is flat-foldable by virtue of Kawasaki theorem [1]. However, the vertex is not developable except when $\alpha=90°$ which makes the sum of panel angles 2π. The configuration space or the folded state of the unit cell can be defined by any of the dihedral or folding angles γ_1, γ_2, γ_3, γ_4, ϕ or ψ (see Fig. S1(a)). These angles are all related to each other through the following equations obtained using the spherical law of cosines applied at the degree-4 vertex:

$$\cos\psi = \cos\alpha\cos(\alpha+\delta)+\sin\alpha\sin(\alpha+\delta)\cos\gamma_1\,, \tag{S1}$$

$$\cos\psi = \cos\alpha\cos(\alpha-\delta)+\sin\alpha\sin(\alpha-\delta)\cos\gamma_3\,, \tag{S2}$$

$$\cos\phi = \cos\alpha\cos(\alpha+\delta)+\sin\alpha\sin(\alpha+\delta)\cos\gamma_2\,, \tag{S3}$$

$$\cos\phi = \cos\alpha\cos(\alpha-\delta)+\sin\alpha\sin(\alpha-\delta)\cos\gamma_4\,. \tag{S4}$$

By decomposing $\gamma_1=\gamma_1'\pm\gamma_1''$, we can further write the following equations using the spherical law of cosines:

$$\cos\alpha = \cos(\alpha+\delta)\cos\phi+\sin(\alpha+\delta)\sin\phi\cos\gamma_1'\,, \tag{S5}$$

$$\cos(\alpha-\delta) = \cos\alpha\cos\phi+\sin\alpha\sin\phi\cos\gamma_1''\,, \tag{S6}$$

which leads to the following expression for γ_1:

$$\gamma_1 = \cos^{-1}\left(\frac{\cos\alpha-\cos(\alpha+\delta)\cos\phi}{\sin(\alpha+\delta)\sin\phi}\right)\pm\cos^{-1}\left(\frac{\cos(\alpha-\delta)-\cos\alpha\cos\phi}{\sin\alpha\sin\phi}\right). \tag{S7}$$

Note that here the sign '$\pm$' depends on whether the crease corresponding to γ_4 is Mountain or Valley fold respectively (see Fig. S1(b),(c)). Finally, using the above equation in Eqn. S1 we obtain the following relation between ϕ and ψ that allows us to study the configuration space:

$$\cos\psi = \cos(\alpha+\delta)\cos\alpha+\sin(\alpha+\delta)\sin\alpha \cos\left[\cos^{-1}\left(\frac{\cos\alpha-\cos(\alpha+\delta)\cos\phi}{\sin(\alpha+\delta)\sin\phi}\right)\pm\cos^{-1}\left(\frac{\cos(\alpha-\delta)-\cos\alpha\cos\phi}{\sin\alpha\sin\phi}\right)\right]. \tag{S8}$$

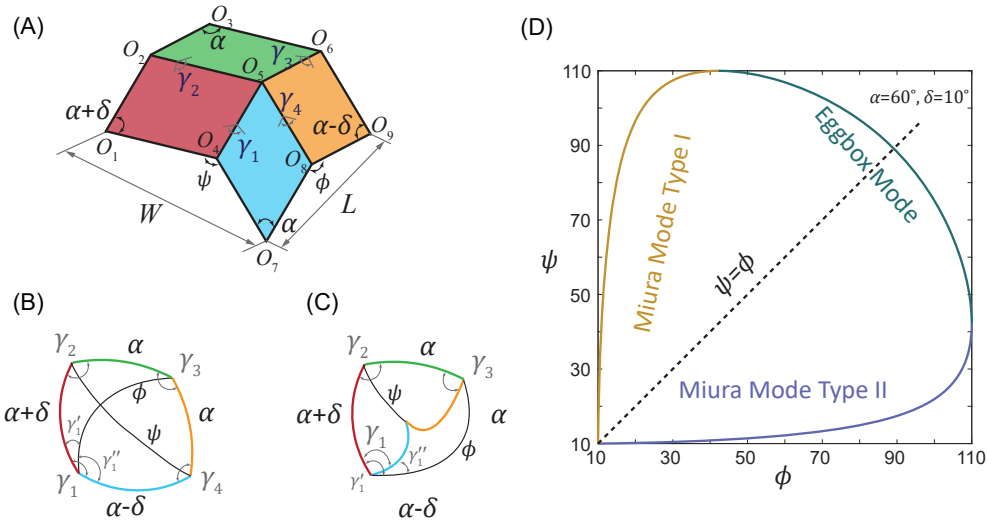

FIG. S1. (A) Geometry of Trimorph unit cell. (B) and (C) are spherical polygonal representations of the O_5 vertex in Eggbox mode and Miura Mode II respectively. (D) Configuration space of the Trimorph unit cell.

A: Configuration space

By simplifying Eqn. S8 using inverse trigonometric identities, we get:

$$\cos\psi = \frac{(\cos\delta - \cos\phi)}{\sin^2\phi}(2\cos^2\alpha \mp \sqrt{(\cos(2\alpha-\delta)-\cos\phi)(\cos(2\alpha+\delta)-\cos\phi)}) + \frac{\cos\phi\sin^2\delta}{\sin^2\phi}\,. \quad \text{(S9)}$$

Here the sign '$\mp$' depends on whether the crease corresponding to γ_4 is Mountain or Valley fold respectively. Further simplification of this equation leads us to a symmetric relation between ϕ and ψ given by,

$$f(\phi,\psi) = 4\cos^2\phi\cos^2\psi - 4(\cos^2\phi+\cos^2\psi) + C(\cos\phi+\cos\psi) + D\cos\phi\cos\psi + E = 0\,, \quad \text{(S10)}$$

where $C = 16\cos^2\alpha\cos\delta$, $D = -8(\cos 2\alpha + \cos^2\delta)$, $E = -\sin^2 2\delta - \cos^2\delta(4+8\cos 2\alpha)$. It can be noted that $f(\phi,\psi) = f(\psi,\phi)$. The symmetry is also evident from Fig. S1(d). This allows us to write

$$\cos\phi = \frac{(\cos\delta - \cos\psi)}{\sin^2\psi}(2\cos^2\alpha \mp \sqrt{(\cos(2\alpha-\delta)-\cos\psi)(\cos(2\alpha+\delta)-\cos\psi)}) + \frac{\cos\psi\sin^2\delta}{\sin^2\psi}\,. \quad \text{(S11)}$$

Here the sign '$\mp$' depends on whether the crease corresponding to γ_3 is Mountain or Valley fold respectively.

B: Vertex coordinates

We consider a coordinate system with origin at vertex O_5 and x-axis along the fold line $\overrightarrow{O_2O_5}$. The xy-plane is assumed to coincide with panel $O_1O_2O_5O_4$ and z-axis is obtained by the right hand rule. The coordinates of the vertices can be obtained using the Rodrigues' rotation formula [2] for finite rotations:

$$\vec{\mathbf{v}}_{rot} = \vec{\mathbf{v}}\cos\beta + (\hat{\mathbf{p}} \times \vec{\mathbf{v}})\sin\beta + \hat{\mathbf{p}}(\hat{\mathbf{p}} \cdot \vec{\mathbf{v}})(1 - \cos\beta)\,, \tag{S12}$$

where $\vec{\mathbf{v}}_{rot}$ is obtained by rotating a vector $\vec{\mathbf{v}}$ about axis of rotation $\hat{\mathbf{p}}$ by an angle β using the right hand rule. The coordinates are obtained as:

$$\begin{aligned}
O_5 &= (0,0,0)\\
O_2 &= (-a,0,0)\\
O_1 &= (-a - a\cos(\alpha+\delta), -a\sin(\alpha+\delta), 0)\\
O_4 &= (-a\cos(\alpha+\delta), -a\sin(\alpha+\delta), 0)\\
O_6 &= (-a\cos\alpha, -a\cos\gamma_2\sin\alpha, -a\sin\gamma_2\sin\alpha)\\
O_3 &= (-a - a\cos\alpha, -a\cos\gamma_2\sin\alpha, -a\sin\gamma_2\sin\alpha)\\
O_8 &= (-a(\cos(\alpha+\delta)\cos\alpha + \sin(\alpha+\delta)\sin\alpha\cos\gamma_1),\\
&\qquad -a(\sin(\alpha+\delta)\cos\alpha - \cos(\alpha+\delta)\sin\alpha\cos\gamma_1), -a(\sin\gamma_1\sin\alpha))\\
O_7 &= (-a\cos(\alpha+\delta) - a(\cos(\alpha+\delta)\cos\alpha + \sin(\alpha+\delta)\sin\alpha\cos\gamma_1),\\
&\qquad -a\sin(\alpha+\delta) - a(\sin(\alpha+\delta)\cos\alpha - \cos(\alpha+\delta)\sin\alpha\cos\gamma_1), -a(\sin\gamma_1\sin\alpha))\\
O_9 &= (-a\cos\alpha - a(\cos(\alpha+\delta)\cos\alpha + \sin(\alpha+\delta)\sin\alpha\cos\gamma_1),\\
&\qquad -a\cos\gamma_2\sin\alpha - a(\sin(\alpha+\delta)\cos\alpha - \cos(\alpha+\delta)\sin\alpha\cos\gamma_1),\\
&\qquad\quad -a\sin\gamma_2\sin\alpha - a(\sin\gamma_1\sin\alpha))
\end{aligned}$$

This coordinate framework allows us to obtain further analytical relations between the dihedral angles. For example, the condition that $\overrightarrow{O_5O_8} \cdot \overrightarrow{O_5O_6} = a^2\cos(\alpha - \delta)$ gives the

following relation between γ_1 and γ_2,

$$f(\gamma_1,\gamma_2) = -\cos(\alpha-\delta) + \cos(\alpha+\delta)\cos^2\alpha + \sin(\alpha+\delta)\sin\alpha\cos\alpha(\cos\gamma_1+\cos\gamma_2) \\ -\cos(\alpha+\delta)\sin^2\alpha\cos\gamma_1\cos\gamma_2 + \sin^2\alpha\sin\gamma_1\sin\gamma_2 = 0\,, \tag{S13}$$

which will be used in a later derivation. Similarly, by choosing a different coordinate system with origin at vertex O_5 and x-axis along the fold line $\overrightarrow{O_6O_5}$, we can use the condition that $\overrightarrow{O_5O_8}\cdot\overrightarrow{O_5O_4} = a^2\cos\alpha$ which gives the following relation between γ_2 and γ_3,

$$-\cos\alpha + \cos(\alpha+\delta)\cos(\alpha-\delta)\cos\alpha \\ +\sin\alpha(\sin(\alpha+\delta)\cos(\alpha-\delta)\cos\gamma_2 + \cos(\alpha+\delta)\sin(\alpha-\delta)\cos\gamma_3) \\ -\cos\alpha\sin(\alpha-\delta)\sin(\alpha+\delta)\cos\gamma_2\cos\gamma_3 + \sin(\alpha-\delta)\sin(\alpha+\delta)\sin\gamma_2\sin\gamma_3 = 0\,. \tag{S14}$$

C: Triclinic angles of the unit cell

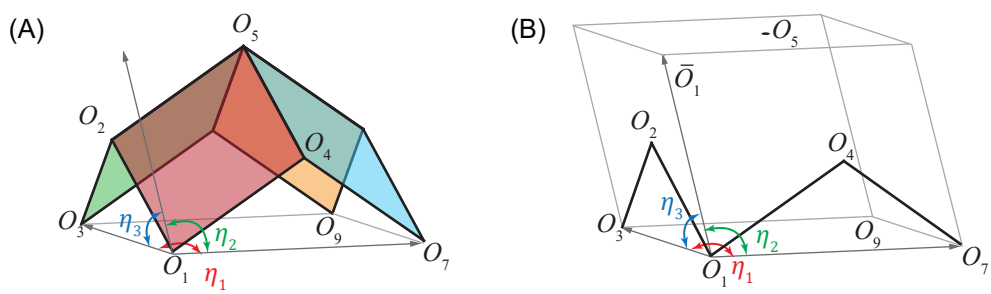

FIG. S2. (A) Triclinic angles of the Trimorph unit cell. (B) Bounding box of the Trimorph unit cell.

The vertices O_1, O_3, O_7 and O_9 are co-planar and form a parallelogram with angle η_1 at O_1 (see Fig. S2(a)). The angle η_1 is calculated as follows:

$$\overrightarrow{O_1O_3}\cdot\overrightarrow{O_1O_7} = LW\cos\eta_1 = 4a^2\sin\frac{\phi}{2}\sin\frac{\psi}{2}\cos\eta_1\,. \tag{S15}$$

The dot product is calculated using the vertex coordinates obtained previously,

$$\begin{aligned}\overrightarrow{O_1O_3}\cdot\overrightarrow{O_1O_7}/(a^2) &= \cos(\alpha+\delta)\cos^2\alpha + \cos(\alpha+\delta) - \cos(\alpha+\delta)\sin^2\alpha\cos\gamma_1\cos\gamma_2 \\ &\quad + \sin^2\alpha\sin\gamma_1\sin\gamma_2 - 2\cos\alpha + \sin(\alpha+\delta)\sin\alpha\cos\alpha(\cos\gamma_1+\cos\gamma_2) \\ &= \cos(\alpha+\delta) + \cos(\alpha-\delta) - 2\cos\alpha\,. \quad \text{(Using Eqn. S13)}\end{aligned} \tag{S16}$$

Using this result in Eqn. S15, we get,

$$\cos\eta_1 = \frac{\cos\alpha(\cos\delta - 1)}{2\sin\frac{\phi}{2}\sin\frac{\psi}{2}}\,. \tag{S17}$$

Equation S17 indicates that η_1 depends on the folded state of the system, and is greater than 90° for $\delta > 0°$, making the base of the unit cell non-orthogonal.

The other two triclinic angles (see Fig. S2(a)) can be evaluated as

$$\cos\eta_2 = \hat{\mathbf{r}}\cdot\overrightarrow{O_1O_7}/W\,,$$
$$\cos\eta_3 = \hat{\mathbf{r}}\cdot\overrightarrow{O_1O_3}/L\,,$$

where $\hat{\mathbf{r}} = [r_x, r_y, r_z]$ is a unit vector along one of the edges $\overrightarrow{O_1\bar{O}_1}$ of the bounding box of the unit cell as shown in Fig. S2(b). The vector $\hat{\mathbf{r}}$ can be obtained by solving the following set of equations.

$$\hat{\mathbf{r}}\cdot(\overrightarrow{O_2O_1}\times\overrightarrow{O_2O_3}) = 0\,,$$
$$\hat{\mathbf{r}}\cdot(\overrightarrow{O_4O_7}\times\overrightarrow{O_4O_1}) = 0\,,$$
$$r_x^2 + r_y^2 + r_z^2 = 1\,.$$

II: In-plane stretching of Trimorph

Figure S3 provides a schematic of the deformation of the base of the unit cell under in-plane stretching of the tessellation. Stretching in one of the $\mathbf{W} = \overrightarrow{O_1O_7}$ or $\mathbf{L} = \overrightarrow{O_1O_3}$ directions results in a deformation in the other direction as well. The inter-dependence of deformations in both these lattice directions can be calculated by looking at the corresponding changes in ϕ and ψ. Using $f(\phi,\psi) = 0$ from Eqn. S10, we have,

$$\mathrm{d}f = \frac{\partial f}{\partial\phi}\mathrm{d}\phi + \frac{\partial f}{\partial\psi}\mathrm{d}\psi = 0 \implies \frac{\mathrm{d}\phi}{\mathrm{d}\psi} = -\frac{\partial f}{\partial\psi}\left(\frac{\partial f}{\partial\phi}\right)^{-1}. \tag{S18}$$

To characterize the deformations of the system during in-plane stretching, we study the ratio of strains: (1) along the lattice directions and (2) along the principal directions. The latter corresponds to the conventional notion of Poisson's ratio where there is no shear strain. However, the former quantity provides a more convenient notion that allows us to gain insight into the in-plane mechanics of the lattice.

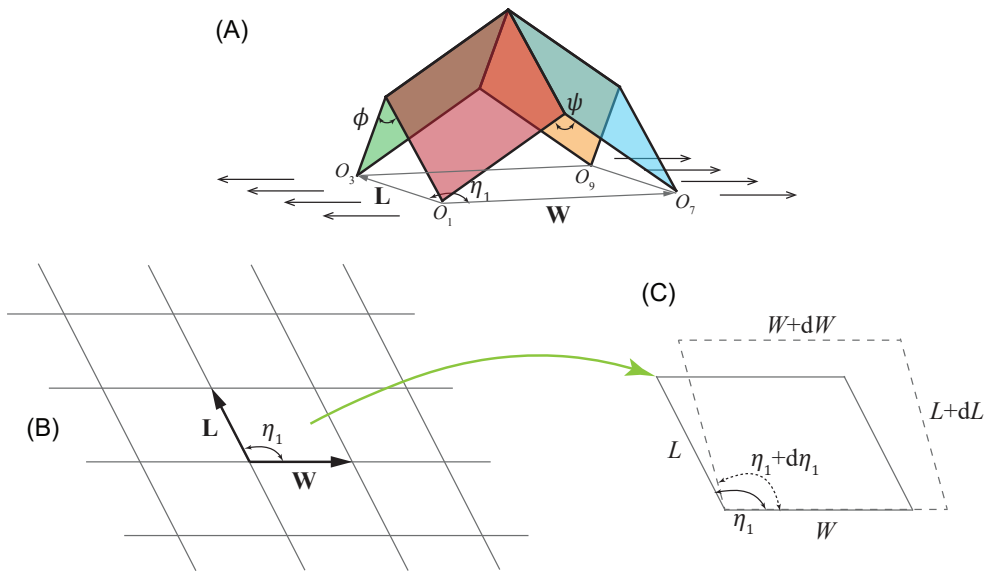

FIG. S3. In-plane stretching of Trimorph unit cell. (a) Extension considered along the **W** direction. (b) 2D schematic of the triclinic tessellation and the lattice vectors **W** and **L**. (c) Shape of a unit cell base before and after the deformation due to in-plane stretching.

A: Lattice Poisson's Ratio (LPR) in stretching

We define Lattice Poisson's Ratio (LPR) in stretching as the ratio of strains along the lattice directions $\varepsilon_L = \mathrm{d}L/L$ and $\varepsilon_W = \mathrm{d}W/W$, given by,

$$\begin{aligned}
\nu^{\ell}_{stretch} &= -\frac{\varepsilon_L}{\varepsilon_W} = -\frac{W}{L}\frac{\mathrm{d}L}{\mathrm{d}\phi}\frac{\mathrm{d}\psi}{\mathrm{d}W}\frac{\mathrm{d}\phi}{\mathrm{d}\psi} \\
L^2 = 4a^2\sin^2\frac{\phi}{2} &\implies \frac{\mathrm{d}L}{\mathrm{d}\phi} = \frac{a^2\sin\phi}{L} \\
W^2 = 4a^2\sin^2\frac{\psi}{2} &\implies \frac{\mathrm{d}W}{\mathrm{d}\psi} = \frac{a^2\sin\psi}{W} \\
\implies \nu^{\ell}_{stretch} &= -\frac{\tan(\psi/2)}{\tan(\phi/2)}\left(\frac{\mathrm{d}\phi}{\mathrm{d}\psi}\right).
\end{aligned}$$

Using the derivative from Eqn. S18, we get

$$\nu^{\ell}_{stretch} = \frac{\sin^2(\psi/2)}{\sin^2(\phi/2)}\left[\frac{(\cos 2\alpha + \cos^2\delta)\cos\phi - 2\cos^2\alpha\cos\delta + \sin^2\phi\cos\psi}{(\cos 2\alpha + \cos^2\delta)\cos\psi - 2\cos^2\alpha\cos\delta + \sin^2\psi\cos\phi}\right]. \tag{S19}$$

We denote $\nu^{\ell}_{stretch}$ as ν_{WL}.

B: Principal Poisson's Ratio (PPR) in stretching

The deformation gradient describing a linear deformation shown in Fig. S3(c) can be obtained as,

$$\mathbf{F} = \begin{bmatrix} (1+\frac{\mathrm{d}W}{W}) & (\frac{\mathrm{d}L}{L}-\frac{\mathrm{d}W}{W})\frac{\cos\eta_1}{\sin\eta_1} - \mathrm{d}\eta_1 \\ 0 & 1+\frac{\mathrm{d}L}{L}+\mathrm{d}\eta_1\frac{\cos\eta_1}{\sin\eta_1} \end{bmatrix} .$$

The infinitesimal strain tensor is calculated as,

$$\begin{aligned} \mathbf{E} &= \frac{1}{2}(\mathbf{F}^T+\mathbf{F}) - \mathbf{I} \\ &= \begin{bmatrix} \frac{\mathrm{d}W}{W} & \frac{1}{2}(\frac{\mathrm{d}L}{L}-\frac{\mathrm{d}W}{W})\frac{\cos\eta_1}{\sin\eta_1} - \frac{\mathrm{d}\eta_1}{2} \\ \frac{1}{2}(\frac{\mathrm{d}L}{L}-\frac{\mathrm{d}W}{W})\frac{\cos\eta_1}{\sin\eta_1} - \frac{\mathrm{d}\eta_1}{2} & \frac{\mathrm{d}L}{L}+\mathrm{d}\eta_1\frac{\cos\eta_1}{\sin\eta_1} \end{bmatrix} \\ &= \begin{bmatrix} \frac{\mathrm{d}W}{\mathrm{d}\psi}\frac{1}{W} & \frac{1}{2}(\frac{\mathrm{d}L}{\mathrm{d}\phi}\frac{\mathrm{d}\phi}{\mathrm{d}\psi}\frac{1}{L}-\frac{\mathrm{d}W}{\mathrm{d}\psi}\frac{1}{W})\frac{\cos\eta_1}{\sin\eta_1} - \frac{\mathrm{d}\eta_1}{\mathrm{d}\psi}\frac{1}{2} \\ \frac{1}{2}(\frac{\mathrm{d}L}{\mathrm{d}\phi}\frac{\mathrm{d}\phi}{\mathrm{d}\psi}\frac{1}{L}-\frac{\mathrm{d}W}{\mathrm{d}\psi}\frac{1}{W})\frac{\cos\eta_1}{\sin\eta_1} - \frac{\mathrm{d}\eta_1}{\mathrm{d}\psi}\frac{1}{2} & \frac{\mathrm{d}L}{\mathrm{d}\phi}\frac{\mathrm{d}\phi}{\mathrm{d}\psi}\frac{1}{L}+\frac{\mathrm{d}\eta_1}{\mathrm{d}\psi}\frac{\cos\eta_1}{\sin\eta_1} \end{bmatrix} \mathrm{d}\psi . \end{aligned} \tag{S20}$$

We define the Principal Poisson's Ratio (PPR) in stretching ($\nu^p_{stretch}$) as the ratio of principal strains calculated as the ratio of the eigenvalues of the above strain tensor at any given folded state of the system.

C: Shear-Normal coupling coefficient

The expression for the strain tensor in Eqn. S20 can be further simplified and expressed in terms of LPR (ν_{WL}) as follows

$$\mathbf{E} = \begin{bmatrix} 1 & -\cot\eta_1 \\ -\cot\eta_1 & (1-\nu_{WL})\cot^2\eta_1 - \nu_{WL} \end{bmatrix} \varepsilon_W \mathrm{d}\psi . \tag{S21}$$

From this, the shear-normal coupling coefficient, defined as the negative ratio of shear strain to the applied normal strain, is given by

$$\zeta = -\frac{2\varepsilon_{WL}}{\varepsilon_W} = 2\cot\eta_1 . \tag{S22}$$

D: Load vs. deformation of Trimorph pattern

The elastic energy of a Trimorph pattern with N_W and N_L number of cells along the **W** and **L** directions, respectively, at a folded state ψ is given by

$$\mathcal{U}(\psi) = N_W(2N_L-1)(\mathcal{U}_1+\mathcal{U}_3) + N_L(2N_W-1)(\mathcal{U}_2+\mathcal{U}_4) , \tag{S23}$$

where $\mathcal{U}_i = \mathcal{U}_i(\gamma_i(\psi), \bar{\gamma}_i, K_F)$ (for $i \in \{1, 2, 3, 4\}$) is the energy stored in crease with dihedral angle γ_i. Here $\bar{\gamma}_i$ are the rest angles and K_F is the crease rotational stiffness. The constitutive relation for the crease given by $M(\gamma_i) = \mathrm{d}\mathcal{U}_i/\mathrm{d}\gamma_i$ can be adopted from nonlinear mechanics of origami [3].

The in-plane uniaxial load required to deform the pattern along the **W** direction is given by

$$\frac{\mathrm{d}\mathcal{U}(\psi)}{\mathrm{d}W} = \frac{\mathrm{d}\mathcal{U}}{\mathrm{d}\psi}\frac{\mathrm{d}\psi}{\mathrm{d}W} = \frac{N_W(2N_L-1)}{a\cos(\psi/2)}\left(\frac{\mathrm{d}\mathcal{U}_1}{\mathrm{d}\psi} + \frac{\mathrm{d}\mathcal{U}_3}{\mathrm{d}\psi}\right) + \frac{N_L(2N_W-1)}{a\cos(\psi/2)}\left(\frac{\mathrm{d}\mathcal{U}_2}{\mathrm{d}\psi} + \frac{\mathrm{d}\mathcal{U}_4}{\mathrm{d}\psi}\right). \quad \text{(S24)}$$

The above equation can be re-written as

$$\begin{aligned}\frac{\mathrm{d}\mathcal{U}(\psi)}{\mathrm{d}W} = &\frac{N_W(2N_L-1)}{a\cos(\psi/2)}\left(M(\gamma_1)\frac{\mathrm{d}\gamma_1}{\mathrm{d}\psi} + M(\gamma_3)\frac{\mathrm{d}\gamma_3}{\mathrm{d}\psi}\right)\\ &+\frac{N_L(2N_W-1)}{a\cos(\psi/2)}\left(M(\gamma_2)\frac{\mathrm{d}\gamma_2}{\mathrm{d}\psi} + M(\gamma_4)\frac{\mathrm{d}\gamma_4}{\mathrm{d}\psi}\right),\end{aligned} \quad \text{(S25)}$$

where

$$\frac{\mathrm{d}\gamma_1}{\mathrm{d}\psi} = \frac{\sin\psi}{\sin\alpha\sin(\alpha+\delta)\sin\gamma_1}, \quad \text{(S26)}$$

$$\frac{\mathrm{d}\gamma_2}{\mathrm{d}\psi} = \frac{\sin\phi}{\sin\alpha\sin(\alpha+\delta)\sin\gamma_2}\frac{\mathrm{d}\phi}{\mathrm{d}\psi}, \quad \text{(S27)}$$

$$\frac{\mathrm{d}\gamma_3}{\mathrm{d}\psi} = \frac{\sin\psi}{\sin\alpha\sin(\alpha-\delta)\sin\gamma_3}, \quad \text{(S28)}$$

$$\frac{\mathrm{d}\gamma_4}{\mathrm{d}\psi} = \frac{\sin\phi}{\sin\alpha\sin(\alpha-\delta)\sin\gamma_4}\frac{\mathrm{d}\phi}{\mathrm{d}\psi}, \quad \text{(S29)}$$

In the above equations, $\mathrm{d}\phi/\mathrm{d}\psi$ can be evaluated using Eqn. S18.

III: Out-of-plane bending of Trimorph

The bending of the origami tessellation can be modeled by allowing the panels to undergo deformation. Previous research has found that imposing infinitesimal rotations (ω_i, $i = 1, 2, 3, 4$) across shorter diagonals of the panels (see Fig. S4(a)) is sufficient to capture first order deformation to define the discrete curvatures of the tessellation [4, 5]. Analogous to in-plane stretching, one can characterize out-of-plane bending deformation through the negative of the ratio of curvatures along either the lattice or the principal directions [6]. Accordingly, we define the Lattice and Principal Poisson's Ratios (LPR and PPR) for bending as the aforementioned ratio of curvatures along corresponding directions.

A: Vertex coordinates after bending

The coordinates of the vertices after application of the infinitesimal rotations are obtained using Rodrigues' rotation formula [2] for small rotations as:

$$
\begin{aligned}
&O_5' = O_5 = (0,0,0)\\
&O_2' = O_2 = (-a,0,0)\\
&O_4' = O_4 = (-a\cos(\alpha+\delta), -a\sin(\alpha+\delta), 0)\\
&O_6' = O_6 = (-a\cos\alpha, -a\cos\gamma_2\sin\alpha, -a\sin\gamma_2\sin\alpha)\\
&O_1' = (-a - a\cos(\alpha+\delta), -a\sin(\alpha+\delta), a^2\sin(\alpha+\delta)\frac{\omega_1}{\ell_1})\\
&O_3' = (-a - a\cos\alpha, -a\cos\gamma_2\sin\alpha + (a^2\sin\gamma_2\sin\alpha)\frac{\omega_2}{\ell_2}, -a\sin\gamma_2\sin\alpha - (a^2\cos\gamma_2\sin\alpha)\frac{\omega_2}{\ell_2})
\end{aligned}
,
$$

where the lengths of the panel diagonals $\overrightarrow{O_2O_4}$, $\overrightarrow{O_2O_6}$, $\overrightarrow{O_6O_8}$, $\overrightarrow{O_4O_8}$ are denoted as ℓ_1, ℓ_2, ℓ_3 and ℓ_4 respectively.

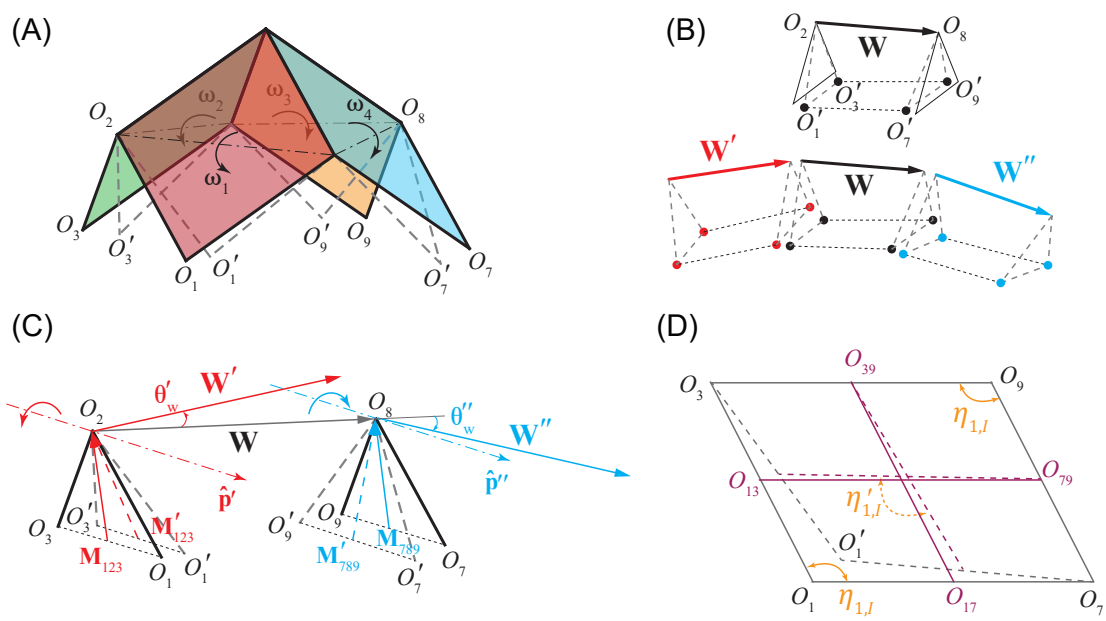

FIG. S4. Out-of-plane bending of Trimorph unit cell. (A) Panel bending through infinitesimal rotations about the diagonals. (B) and (C) Triangular faces along the **W** direction before and after bending. (D) Parallelogram shaped base of the Trimorph unit cell and its perturbed shape due to a single panel bending.

B: Constraints on bending rotations

The infinitesimal rotations on the four panels of the unit cell add four additional degrees of freedom (DOF) and have to be constrained in an appropriate way to simulate the bending mode of deformation. We impose two conditions that reduce the DOF leading to a unique bending mode: (i) Tessellation Boundary Condition (TBC), and (ii) Frame constraint.

1: Tessellation Boundary Condition

This constraint ensures that the periodic boundary conditions on the unit cell are still satisfied after bending deformations are applied. For this, we impose, $\angle O_1'O_2'O_3' = \angle O_7'O_8'O_9'$ (see Fig. S4(b),(c)) and $\angle O_1'O_4'O_7' = \angle O_3'O_6'O_9'$. This translates as $\overrightarrow{O_2O_3}\cdot\overrightarrow{O_2O_1} = \overrightarrow{O_8O_9}\cdot\overrightarrow{O_8O_7}$ and $\overrightarrow{O_4O_1}\cdot\overrightarrow{O_4O_7} = \overrightarrow{O_6O_9}\cdot\overrightarrow{O_6O_3}$ respectively. Since, the angles are independent of the choice of coordinate system we can choose the axis conveniently within the plane of each of the four panels while we calculate the corresponding dot products mentioned above. Evaluating the above conditions we arrive at the following constraints for the infinitesimal rotations,

$$\sin(\alpha+\delta)\sin\alpha\sin\gamma_2\left(\frac{\omega_2}{\ell_2}+\frac{\omega_1}{\ell_1}\right) = \sin(\alpha-\delta)\sin\alpha\sin\gamma_4\left(\frac{\omega_3}{\ell_3}+\frac{\omega_4}{\ell_4}\right), \tag{S30}$$

$$\sin(\alpha+\delta)\sin\alpha\sin\gamma_1\left(\frac{\omega_4}{\ell_4}+\frac{\omega_1}{\ell_1}\right) = \sin(\alpha-\delta)\sin\alpha\sin\gamma_3\left(\frac{\omega_3}{\ell_3}+\frac{\omega_2}{\ell_2}\right). \tag{S31}$$

2: Frame constraint

We want to ensure that the frame (local co-ordinate system) in the bent configuration is unchanged. For this, the base of the parallelogram $O_1O_3O_9O_7$ should not change in shape (no shear or twist) so as to give a bending deformation mode. We define $\angle O_3O_1O_7 = \eta_{1,I}$, $\angle O_7O_9O_3 = \eta_{1,III}$, $\angle O_1O_7O_9 = \eta_{1,IV}$ and $\angle O_1O_3O_9 = \eta_{1,II}$ before applying the infinitesimal rotations, where, $\eta_{1,I} = \eta_{1,III} = \pi - \eta_{1,II} = \pi - \eta_{1,IV} = \eta_1$. Infinitesimal rotation ω_1 takes O_1 to O_1' and the corresponding angle between the mid lines $\eta_{1,I}$ becomes $\eta_{1,I}'$ (see Fig. S4(d)). After all the rotations are applied, the parallelogram angle (between the mid lines $\overrightarrow{O_{17}O_{39}}$ and $\overrightarrow{O_{13}O_{79}}$) changes from η_1 to η_1'. (Note that O_{17} is obtained as mid point of O_1 and O_7.)

The angle η_1' of the unit cell base in the bent configuration depends on the positions of

the vertices O'_1, O'_3, O'_9 and O'_7 which should satisfy the following condition,

$$\eta'_1 - \eta_1 = \Delta\eta_1(\omega_1, \omega_2, \omega_3, \omega_4) = \Delta\eta_1(\omega_1) + \Delta\eta_1(\omega_2) + \Delta\eta_1(\omega_3) + \Delta\eta_1(\omega_4) = 0\,,$$

where $\Delta\eta_1(\omega_i) = -(\cos\eta'_{1,i} - \cos\eta_{1,i})/\sin\eta_i$, for $i = I, II, III, IV$. Since, $\sin\eta_{1,I} = \sin\eta_{1,II} = \sin\eta_{1,III} = \sin\eta_{1,IV} = \sin\eta_1$, the constraint becomes:

$$(\cos\eta'_{1,I} - \cos\eta_{1,I}) + (\cos\eta'_{1,II} - \cos\eta_{1,II}) + (\cos\eta'_{1,III} - \cos\eta_{1,III}) + (\cos\eta'_{1,IV} - \cos\eta_{1,IV}) = 0\,.$$

This can be calculated as:

$$\begin{aligned}&(\overrightarrow{O_{1'7}O_{39}} \cdot \overrightarrow{O_{1'3}O_{79}} - \overrightarrow{O_{17}O_{39}} \cdot \overrightarrow{O_{13}O_{79}}) + (\overrightarrow{O_{17}O_{3'9}} \cdot \overrightarrow{O_{13'}O_{79}} - \overrightarrow{O_{17}O_{39}} \cdot \overrightarrow{O_{13}O_{79}})\\ &+(\overrightarrow{O_{17'}O_{39}} \cdot \overrightarrow{O_{13}O_{7'9}} - \overrightarrow{O_{17}O_{39}} \cdot \overrightarrow{O_{13}O_{79}}) + (\overrightarrow{O_{17}O_{39'}} \cdot \overrightarrow{O_{13}O_{79}} - \overrightarrow{O_{17}O_{39}} \cdot \overrightarrow{O_{13}O_{79'}}) = 0\,.\end{aligned}$$

Since, the constraint is just a summation of change in angles, each of the above terms can be calculated by using different coordinate system that will allow simple expressions as given below:

$$\begin{aligned}\overrightarrow{O_{1'7}O_{39}} \cdot \overrightarrow{O_{1'3}O_{79}} - \overrightarrow{O_{17}O_{39}} \cdot \overrightarrow{O_{13}O_{79}} &= \sin(\alpha+\delta)\sin\alpha(\sin\gamma_1 + \sin\gamma_2)\frac{\omega_1}{\ell_1}(a^3/2)\\ \overrightarrow{O_{17}O_{3'9}} \cdot \overrightarrow{O_{13'}O_{79}} - \overrightarrow{O_{17}O_{39}} \cdot \overrightarrow{O_{13}O_{79}} &= -\sin\alpha(\sin(\alpha+\delta)\sin\gamma_2 + \sin(\alpha-\delta)\sin\gamma_3)\frac{\omega_2}{\ell_2}(a^3/2)\\ \overrightarrow{O_{17}O_{39'}} \cdot \overrightarrow{O_{13}O_{79}} - \overrightarrow{O_{17}O_{39}} \cdot \overrightarrow{O_{13}O_{79'}} &= \sin(\alpha-\delta)\sin\alpha(\sin\gamma_3 + \sin\gamma_4)\frac{\omega_3}{\ell_3}(a^3/2)\\ \overrightarrow{O_{17'}O_{39}} \cdot \overrightarrow{O_{13}O_{7'9}} - \overrightarrow{O_{17}O_{39}} \cdot \overrightarrow{O_{13}O_{79}} &= -\sin\alpha(\sin(\alpha-\delta)\sin\gamma_4 + \sin(\alpha+\delta)\sin\gamma_1)\frac{\omega_4}{\ell_4}(a^3/2)\end{aligned}$$

Finally, the frame constraint is given by:

$$\begin{aligned}&\sin(\alpha+\delta)\sin\alpha(\sin\gamma_1 + \sin\gamma_2)\frac{\omega_1}{\ell_1} - \sin\alpha(\sin(\alpha+\delta)\sin\gamma_2 + \sin(\alpha-\delta)\sin\gamma_3)\frac{\omega_2}{\ell_2}\\ &+\sin(\alpha-\delta)\sin\alpha(\sin\gamma_3 + \sin\gamma_4)\frac{\omega_3}{\ell_3} - \sin\alpha(\sin(\alpha-\delta)\sin\gamma_4 + \sin(\alpha+\delta)\sin\gamma_1)\frac{\omega_4}{\ell_4} = 0\,.\end{aligned} \tag{S32}$$

3: Relation between rotations

Solving the three constraints (Eqns. S30, S31, S32), we arrive at the following relations between the rotations that satisfy the constraints.

$$\begin{aligned}
\frac{\omega_2}{\ell_2} &= \left(\frac{\sin(\alpha+\delta)\sin\gamma_1}{\sin(\alpha-\delta)\sin\gamma_3}\right)\frac{\omega_1}{\ell_1} \\
\frac{\omega_4}{\ell_4} &= \left(\frac{\sin(\alpha+\delta)\sin\gamma_2}{\sin(\alpha-\delta)\sin\gamma_4}\right)\frac{\omega_1}{\ell_1} \\
\frac{\omega_3}{\ell_3} &= \left(\frac{\sin^2(\alpha+\delta)\sin\gamma_2\sin\gamma_1}{\sin^2(\alpha-\delta)\sin\gamma_4\sin\gamma_3}\right)\frac{\omega_1}{\ell_1}
\end{aligned} \tag{S33}$$

C: Bending curvatures

We characterize the bent configuration of a tessellation through a discrete description of space curves along the lattice directions $\mathbf{W}$ and $\mathbf{L}$ embedded in a parameterized surface. The normal curvature of this discrete surface formed by the bent tessellation can be evaluated through the second fundamental form at a reference unit cell about which the bending is concentrated. Within the $\{\hat{\mathbf{W}}, \hat{\mathbf{L}}\}$ basis, the normal curvature along any lattice direction is calculated as the normal component of the change in the lattice vector per unit length. Here, "$\hat{}$" represents the unit normalized vectors. We denote $\mathbf{M}_{123}$, $\mathbf{M}_{789}$, $\mathbf{M}_{147}$ and $\mathbf{M}_{369}$ as the medians (which are also the altitudes) of the triangles $O_1O_2O_3$, $O_7O_8O_9$, $O_1O_4O_7$ and $O_3O_6O_9$ respectively (see Fig. S4(c)). As the unit cell undergoes bending, $\mathbf{M}_{123}$ rotates to $\mathbf{M}'_{123}$ by a small angle θ'_W about an axes $\hat{\mathbf{p}}'$, and $\mathbf{M}_{789}$ rotates to $\mathbf{M}'_{789}$ by a small angle θ''_W about an axes $\hat{\mathbf{p}}''$. Correspondingly, $\mathbf{W}$ rotates to $\mathbf{W}'$ and $\mathbf{W}''$ respectively as shown in Fig. S4(c). Therefore, we can write

$$\hat{\mathbf{W}} - \hat{\mathbf{W}}' = \theta'_W \hat{\mathbf{p}}' \times \hat{\mathbf{W}} = (\hat{\mathbf{M}}'_{123} \times \hat{\mathbf{M}}_{123}) \times \hat{\mathbf{W}}\,, \tag{S34}$$

$$\hat{\mathbf{W}}'' - \hat{\mathbf{W}} = -\theta''_W \hat{\mathbf{p}}'' \times \hat{\mathbf{W}} = -(\hat{\mathbf{M}}'_{789} \times \hat{\mathbf{M}}_{789}) \times \hat{\mathbf{W}}\,. \tag{S35}$$

Combining these two equations, we get

$$\hat{\mathbf{W}}'' - \hat{\mathbf{W}}' = \Big[(\hat{\mathbf{M}}'_{123} \times \hat{\mathbf{M}}_{123}) - (\hat{\mathbf{M}}'_{789} \times \hat{\mathbf{M}}_{789})\Big] \times \hat{\mathbf{W}}\,. \tag{S36}$$

Using a similar description, we can also get

$$\hat{\mathbf{L}}'' - \hat{\mathbf{L}}' = \Big[(\hat{\mathbf{M}}'_{147} \times \hat{\mathbf{M}}_{147}) - (\hat{\mathbf{M}}'_{369} \times \hat{\mathbf{M}}_{369})\Big] \times \hat{\mathbf{W}}\,. \tag{S37}$$

The normal curvatures along $\mathbf{W}$ and $\mathbf{L}$ directions can then be defined as,

$$\kappa_W = \frac{(\mathbf{W}'' - \mathbf{W}') \cdot \hat{\mathbf{n}}}{W^2}\,, \tag{S38}$$

$$\kappa_L = \frac{(\mathbf{L}'' - \mathbf{L}') \cdot \hat{\mathbf{n}}}{L^2}\,, \tag{S39}$$

where $\hat{\mathbf{n}} = (\mathbf{W} \times \mathbf{L})/|\mathbf{W} \times \mathbf{L}|$. Therefore, the curvatures can be calculated as,

$$\kappa_W = \frac{\left[(\hat{\mathbf{M}}'_{123} \times \hat{\mathbf{M}}_{123}) \times \hat{\mathbf{W}} - (\hat{\mathbf{M}}'_{789} \times \hat{\mathbf{M}}_{789}) \times \hat{\mathbf{W}}\right] \cdot \hat{\mathbf{n}}}{W}\,, \tag{S40}$$

$$\kappa_L = \frac{\left[(\hat{\mathbf{M}}'_{147} \times \hat{\mathbf{M}}_{147}) \times \hat{\mathbf{L}} - (\hat{\mathbf{M}}'_{369} \times \hat{\mathbf{M}}_{369}) \times \hat{\mathbf{L}}\right] \cdot \hat{\mathbf{n}}}{L}\,. \tag{S41}$$

However, evaluating the above expressions analytically becomes very cumbersome using a single coordinate system for all the vertices. Hence, we re-write the above equations so that each of the scalar terms would be independent of the choice of coordinate system and can be calculated by suitably modifying the axes as discussed previously. Finally, we have the following equations to calculate the curvatures,

$$\kappa_W = \frac{[(\mathbf{M}'_{123} \times \mathbf{M}_{123}) \times \mathbf{W}_{123}] \cdot (\mathbf{W}_{123} \times \mathbf{L}_{123}) - [(\mathbf{M}'_{789} \times \mathbf{M}_{789}) \times \mathbf{W}_{789}] \cdot (\mathbf{W}_{789} \times \mathbf{L}_{789})}{8a^5 \sin^2\frac{\psi}{2} \sin\frac{\phi}{2} \cos^2\frac{\phi}{2} \cos\eta_1}\,,$$

$$\kappa_L = \frac{[(\mathbf{M}'_{147} \times \mathbf{M}_{147}) \times \mathbf{L}_{147}] \cdot (\mathbf{W}_{147} \times \mathbf{L}_{147}) - [(\mathbf{M}'_{369} \times \mathbf{M}_{369}) \times \mathbf{L}_{369}] \cdot (\mathbf{W}_{369} \times \mathbf{L}_{369})}{8a^5 \sin^2\frac{\phi}{2} \sin\frac{\psi}{2} \cos^2\frac{\psi}{2} \cos\eta_1}\,,$$

where

$$\mathbf{W}_{123} = [a(1-\cos\psi), -a(\cos\alpha\sin(\alpha+\delta) - \cos\gamma_1\cos(\alpha+\delta)\sin\alpha), -a\sin\alpha\sin\gamma_1]$$

$$\mathbf{L}_{123} = [a(\cos(\alpha+\delta) - \cos\alpha), a(\sin(\alpha+\delta) - \cos\gamma_2\sin\alpha), -a\sin\alpha\sin\gamma_2]$$

$$\begin{aligned}\frac{(\mathbf{M}'_{123} \times \mathbf{M}_{123})}{(\frac{a^3}{4})} = [&\frac{\omega_1}{\ell_1}\sin(\alpha+\delta)(\sin(\alpha+\delta) + \cos\gamma_2\sin\alpha) - \frac{\omega_2}{\ell_2}\sin\alpha(\sin\alpha + \cos\gamma_2\sin(\alpha+\delta)),\\ &-\frac{\omega_1}{\ell_1}\sin(\alpha+\delta)(\cos(\alpha+\delta) + \cos\alpha) + \frac{\omega_2}{\ell_2}\sin\alpha\cos\gamma_2(\cos(\alpha+\delta) + \cos\alpha),\\ &\frac{\omega_2}{\ell_2}\sin\alpha\sin\gamma_2(\cos(\alpha+\delta) + \cos\alpha)]\end{aligned}$$

$$\mathbf{W}_{789} = -[a(1-\cos\psi), -a(\cos\alpha\sin(\alpha-\delta) - \cos\gamma_3\cos(\alpha-\delta)\sin\alpha), -a\sin\alpha\sin\gamma_3]$$

$$\mathbf{L}_{789} = -[a(\cos(\alpha-\delta) - \cos\alpha), a(\sin(\alpha-\delta) - \cos\gamma_4\sin\alpha), -a\sin\alpha\sin\gamma_4]$$

$$\begin{aligned}\frac{(\mathbf{M}'_{789} \times \mathbf{M}_{789})}{(\frac{a^3}{4})} = [&\frac{\omega_3}{\ell_3}\sin(\alpha-\delta)(\sin(\alpha-\delta) + \cos\gamma_4\sin\alpha) - \frac{\omega_4}{\ell_4}\sin\alpha(\sin\alpha + \cos\gamma_4\sin(\alpha-\delta)),\\ &-\frac{\omega_3}{\ell_3}\sin(\alpha-\delta)(\cos(\alpha-\delta) + \cos\alpha) + \frac{\omega_4}{\ell_4}\sin\alpha\cos\gamma_4(\cos(\alpha-\delta) + \cos\alpha),\\ &\frac{\omega_4}{\ell_4}\sin\alpha\sin\gamma_4(\cos(\alpha-\delta) + \cos\alpha)]\end{aligned}$$

$$\mathbf{L}_{143} = [a(1-\cos\phi), -a(\cos(\alpha-\delta)\sin\alpha - \cos\gamma_4\cos\alpha\sin(\alpha-\delta)), -a\sin(\alpha-\delta)\sin\gamma_4]$$

$$\mathbf{W}_{143} = -[a(\cos\alpha - \cos(\alpha+\delta)), a(\sin\alpha - \cos\gamma_1\sin(\alpha+\delta)), -a\sin(\alpha+\delta)\sin\gamma_1]$$

$$\begin{aligned}\frac{(\mathbf{M}'_{143}\times\mathbf{M}_{143})}{(\frac{a^3}{4})} = [&\frac{\omega_4}{\ell_4}\sin\alpha(\sin\alpha+\cos\gamma_1\sin(\alpha+\delta)) - \frac{\omega_1}{\ell_1}\sin(\alpha+\delta)(\sin(\alpha+\delta)+\cos\gamma_1\sin\alpha),\\ &-\frac{\omega_4}{\ell_4}\sin\alpha(\cos\alpha+\cos(\alpha+\delta)) + \frac{\omega_1}{\ell_1}\sin(\alpha+\delta)\cos\gamma_1(\cos\alpha+\cos(\alpha+\delta)),\\ &\frac{\omega_1}{\ell_1}\sin(\alpha+\delta)\sin\gamma_1(\cos\alpha+\cos(\alpha+\delta))]\end{aligned}$$

$$\mathbf{L}_{369} = [-a(1-\cos\phi), a(\cos(\alpha+\delta)\sin\alpha - \cos\gamma_2\cos\alpha\sin(\alpha+\delta)), a\sin(\alpha+\delta)\sin\gamma_2]$$

$$\mathbf{W}_{369} = [a(\cos\alpha - \cos(\alpha-\delta)), a(\sin\alpha - \cos\gamma_3\sin(\alpha-\delta)), -a\sin(\alpha-\delta)\sin\gamma_3]$$

$$\begin{aligned}\frac{(\mathbf{M}'_{369}\times\mathbf{M}_{369})}{(\frac{a^3}{4})} = [&\frac{\omega_2}{\ell_2}\sin\alpha(\sin\alpha+\cos\gamma_3\sin(\alpha-\delta)) - \frac{\omega_3}{\ell_3}\sin(\alpha-\delta)(\sin(\alpha-\delta)+\cos\gamma_3\sin\alpha),\\ &-\frac{\omega_2}{\ell_2}\sin\alpha(\cos\alpha+\cos(\alpha-\delta)) + \frac{\omega_3}{\ell_3}\sin(\alpha-\delta)\cos\gamma_3(\cos\alpha+\cos(\alpha-\delta)),\\ &\frac{\omega_3}{\ell_3}\sin(\alpha-\delta)\sin\gamma_3(\cos\alpha+\cos(\alpha-\delta))]\end{aligned}$$

The infinitesimal rotations ω_i in the above expressions can all be reduced in terms of ω_1 by using Eqns. S33. We shall characterize the bending response of the Trimorph system through the ratio of curvatures along (i) lattice directions and (ii) principal directions.

D: Lattice Poisson's Ratio (LPR) in bending

We define LPR in bending as the ratio of curvatures along the tessellation directions:

$$\nu^{\ell}_{bend} = -\frac{\kappa_L}{\kappa_W}\,,$$

which can be analytically evaluated as

$$\nu^{\ell}_{bend} = -\frac{\sin\frac{\psi}{2}\cos^2\frac{\phi}{2}}{\sin\frac{\phi}{2}\cos^2\frac{\psi}{2}}\left[\frac{[(\mathbf{M}'_{147}\times\mathbf{M}_{147})\times\mathbf{L}_{147}]\cdot(\mathbf{W}_{147}\times\mathbf{L}_{147}) - [(\mathbf{M}'_{369}\times\mathbf{M}_{369})\times\mathbf{L}_{369}]\cdot(\mathbf{W}_{369}\times\mathbf{L}_{369})}{[(\mathbf{M}'_{123}\times\mathbf{M}_{123})\times\mathbf{W}_{123}]\cdot(\mathbf{W}_{123}\times\mathbf{L}_{123}) - [(\mathbf{M}'_{789}\times\mathbf{M}_{789})\times\mathbf{W}_{789}]\cdot(\mathbf{W}_{789}\times\mathbf{L}_{789})}\right]. \tag{S42}$$

E: Principal Poisson's Ratio (PPR) in bending

In order to calculate the principal curvatures, we need to look at the matrix representation of the differential of the Gauss map [7] within the $\{\hat{\mathbf{W}}, \hat{\mathbf{L}}\}$ basis given by,

$$\mathrm{d}\hat{\mathbf{n}} = -\begin{pmatrix} e & f \\ f & g \end{pmatrix} \begin{pmatrix} E & F \\ F & G \end{pmatrix}^{-1} , \tag{S43}$$

where E, F, G and e, f, g are the coefficients of the first (I) and second (II) fundamental forms respectively in the basis $\{\hat{\mathbf{W}}, \hat{\mathbf{L}}\}$. For example,

$$I(\hat{\mathbf{W}}) = \hat{\mathbf{W}} \cdot \hat{\mathbf{W}} , \tag{S44}$$

$$II(\hat{\mathbf{W}}) = \hat{\mathbf{W}} \cdot \mathrm{d}\hat{\mathbf{n}}(\hat{\mathbf{W}}) . \tag{S45}$$

These coefficients are given by,

$$E = \hat{\mathbf{W}} \cdot \hat{\mathbf{W}} = 1 , \qquad F = \hat{\mathbf{W}} \cdot \hat{\mathbf{L}} = \cos\eta_1 , \qquad G = \hat{\mathbf{L}} \cdot \hat{\mathbf{L}} = 1 ,$$
$$e = \frac{\mathrm{d}\hat{\mathbf{W}}}{\mathrm{d}W} \cdot \hat{\mathbf{n}} = \kappa_W , \qquad f = \frac{\mathrm{d}\hat{\mathbf{W}}}{\mathrm{d}L} \cdot \hat{\mathbf{n}} = \frac{\mathrm{d}\hat{\mathbf{L}}}{\mathrm{d}W} \cdot \hat{\mathbf{n}} = 0 , \qquad g = \frac{\mathrm{d}\hat{\mathbf{L}}}{\mathrm{d}L} \cdot \hat{\mathbf{n}} = \kappa_L .$$

By substituting the above expressions we get,

$$\mathrm{d}\hat{\mathbf{n}} = -\frac{1}{\sin^2\eta_1} \begin{pmatrix} \kappa_W & -\kappa_W \cos\eta_1 \\ -\kappa_L \cos\eta_1 & \kappa_L \end{pmatrix} , \tag{S46}$$

with the eigenvalues or the principal curvatures given by,

$$\kappa_p = \frac{-(\kappa_W + \kappa_L) \pm \sqrt{(\kappa_W + \kappa_L)^2 - 4\kappa_W \kappa_L \sin^2\eta_1}}{2\sin^2\eta_1} . \tag{S47}$$

For an orthogonal lattice with $\eta_1 = 90°$, it can be seen from the above expression that the principal curvatures are κ_W, κ_L. The principal curvatures of the bent configuration are given by the eigenvalues of the matrix $\mathrm{d}\hat{\mathbf{n}}$. The negative of the ratio of these principal curvatures gives the PPR in bending (ν^p_{bend}).

IV: Comparison of Poisson's ratios in stretching and bending

In Fig. S5, we compare LPR and PPR for various folded states in stretching and bending. We note that the Poisson's ratio values of Trimorph metamaterial are unbounded [8]. We find that similar to previous studies involving other origami patterns [4, 5], Trimorph also

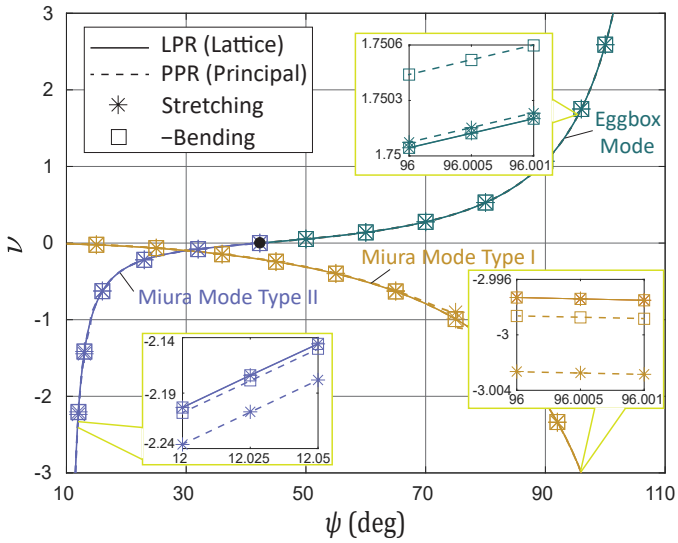

FIG. S5. Comparison of analytically calculated Poisson's ratios in stretching and bending, along lattice and principal directions. The insets show the mismatch between stretching and bending for Principal Poisson's Ratio. The results correspond to $\alpha = 60°$ and $\delta = 10°$.

exhibits the unique property that the bending and stretching Poisson's ratios are equal and opposite, when measured along the lattice directions. Although we did not do analytical verification for the Trimorph pattern, we have performed extended precision calculations up to 500 decimals to verify the claim. On the other hand, we found that such a relation does not hold true for Poisson's ratios measured along the principal directions.

V: Extended explanation about tristability and multistability

Here we elaborate on how to find the rest angles of γ_1 and γ_2 to obtain the tristable Trimorph unit cell. Due to the symmetry between γ_1 and γ_2, we know that configuration (2') in Fig. 6A of the main text happens when $\gamma_1 = \gamma_2$. When $\gamma_1 = \gamma_2$, we know that $\gamma_3 = \gamma_4$, and $\phi = \psi$. This special configuration is defined by:

$$\cos\gamma_{3,(2')} = \frac{\cot(\alpha)\sin(\alpha-\delta) - \csc(\alpha)\sin(\delta) - 1}{\cos(\alpha-\delta)+1}, \tag{S48}$$

and consequently,

$$\cos\gamma_{1,(2')} = \frac{\cos\gamma_{3,(2')}\sin(\alpha-\delta) + 2\cos\alpha\sin\delta}{\sin(\alpha+\delta)}. \tag{S49}$$

Since configurations (1'), (2'), and (3') are of the same energy level, on Fig. 6A, the three corresponding points are on the same circle of energy contour. The center of this circle

marks the rest angles: $\bar{\gamma_1}$ and $\bar{\gamma_2}$, and we know that $\bar{\gamma_1} = \bar{\gamma_2}$ due to symmetry. The other two stable configurations (1') and (3') are the solutions of two nonlinear equations. The first equation is Eq. (S13), which states that (1') and (3') must be on the kinematic path of the Trimorph origami. The second equation is that the distance from (1') or (3') to the center is the same as from (2'), which is already known:

$$(\gamma_1 - \bar{\gamma_1})^2 + (\gamma_2 - \bar{\gamma_1})^2 = 2(\gamma_{1,(2')} - \bar{\gamma_1})^2. \tag{S50}$$

Because the center of the energy contour lies on both the line of $\gamma_1 = \gamma_2$ and the line that is normal to the kinematic path, we can solve for it for any point on the kinematic path:

$$\bar{\gamma_1} = \frac{k_p \gamma_1 - \gamma_2}{k_p - 1}\,, \tag{S51}$$

where k_p is the slope of the normal direction of the kinematic path for any point (γ_1, γ_2) on the path. Let $f(\gamma_1, \gamma_2)$ be the left hand side of Eq. (S13), we obtain k_p as:

$$k_p = \frac{\partial f(\gamma_1, \gamma_2)/\partial \gamma_2}{\partial f(\gamma_1, \gamma_2)/\partial \gamma_1}\,. \tag{S52}$$

Plugging Eq. (S51) into Eq. (S50), and solving the two nonlinear equations numerically, i.e., Eq. (S50) and Eq. (S13), we can obtain the locations of points (1') and (3'), as well as the location of the center, on the γ_1-γ_2 graph.

When we explore the multistable states of the 2D tessellations of the Trimorph origami, we can introduce inhomogeneity by hybridizing the eggbox and Miura modes. It is noted that although the Miura mode unit cells and eggbox mode unit cells can exist compatibly in the same tessellation, their primitive vectors are different, as demonstrated in Fig. S6.

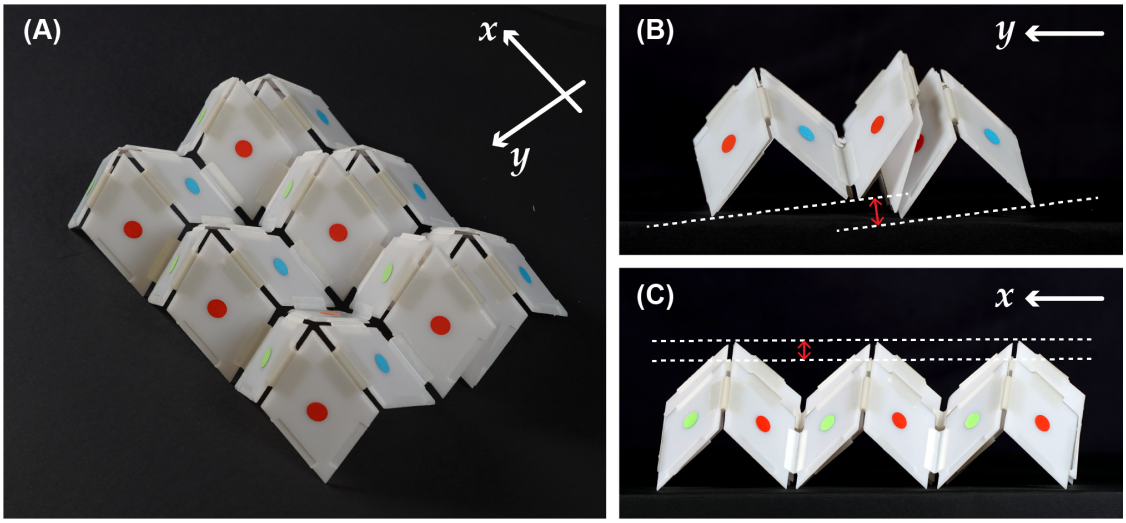

FIG. S6. (A-C) Change of primitive vectors between the eggbox and Miura modes. Owing to the middle row of unit cells in Miura mode, the two rows in eggbox mode do not share the same base plane. The white dashed lines indicates the bases (defined by primitive vectors) on the eggbox mode rows, and the red arrow shows the mismatch between these two bases.

VI: Fabrication of physical prototypes

Three types of triclinic unit cells were designed to create the multistable 2D tessellation, to carry out the Poisson's ratio quantitative experiments, and to realize the 3D metamaterials.

A: Trimorph unit cell, 1D assembly, and 2D tessellation

The 2D (3×3) multistable tessellation was obtained by assembling 9 rigid bimorph origami unit cells. Each unit cell comprises 4 rigid panels jointed together by 4 hinges, 2 elastic and 2 free. Both panels and hinges were designed to mimic as much as possible the ideal unit cell investigated theoretically characterised by the geometrical parameters $a = c = 40$ mm and $\alpha = 60°$ and $\delta = 10°$. Therefore, the panels composing the unit cell have opposite acute interior angles of 50°, 70° and 60°. Specific seats were engraved on the panels to duly housing the hinges and permit the perfect assembly of the unit cell and of the 2D tessellation. The depth of the seats, the actual dimension of panels, and the thickness of the rubber hinges were tailored in a way that, when jointed, the intersection line of the median plane of each panel is very close to the rotation axis of the hinges (maximum tolerance of 1.1 mm), as shown in the sketch of Figs. S7(A) and (B). This is a fundamental condition so that the unit cell, and then the tessellation, exhibit the tristable behavior. In fact, origami-based mechanisms require precision to function as theoretically predicted. For this purpose, a parametric design process was carried out in SolidWorks® by varying the main geometrical parameters, e.g. depth of the seats and thickness of the rubber hinges. Each cell panel was milled from a 2 mm thick PC (Makrolon® Polycarbonate, E=2300 MPa, by Bayer) sheet with a Roland EGX-600 CNC 3-axes engraving machine (accuracy 10 μm). The free hinges (hinge type I in Fig. S7(C)) were cut from a 1 mm thick white Polypropylene sheet using the same milling machine used for the PC panels. Polypropylene was selected because it has the required folding performance and fatigue resistance. This allowed creating very thin (0.2 mm) folding lines giving rise to zero energy hinges, namely almost perfect free hinges, as depicted in Fig. S7(C). Such folding lines were obtained by a ball end mill (radius 1 mm) mounted on the milling machine. The elastic hinges, shown in Fig. S7(C), were realised by cutting a silicon rubber solid (600 mm × 30 mm × 40 mm) with a Roland MDX-540 4-axes CNC engraving machine (accuracy 20 μm), which has rest angle of 62.434 deg (1.0897 rad),

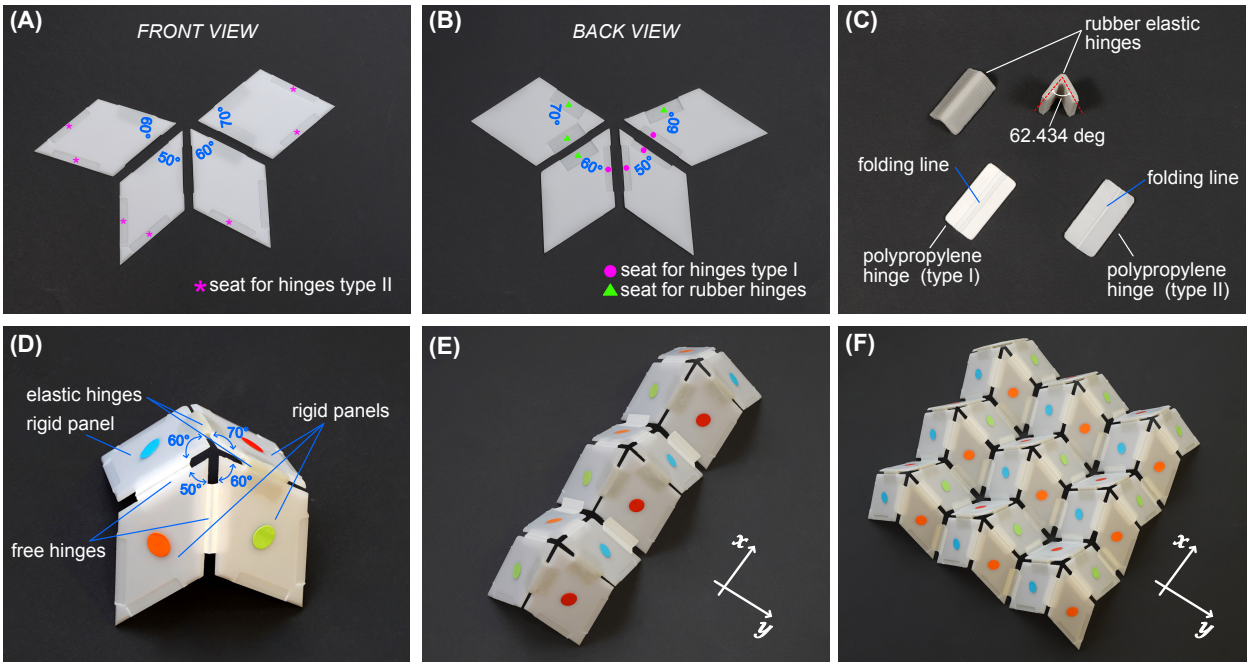

Fig. S7. Front view (A) and back view (B) of the rigid panels composing the triclinic tristable unit cell. In the figure, the details of the seats to duly housing the hinges are also highlighted. (C) Details of the hinges used to build the unit cell (rubber hinges and type I polypropylene hinges), the 1D and 2D tessellation (type II polypropylene hinges). (D) Assembled tristable unit cell. The colored paper disks (10 mm in diameter) indicate the unit cell elements with acute interior angles of 50 deg (orange), 60 deg (green and blue), and 70 deg (red). (E) 1D (3 ×1) assembly. (F) 2D tessellation (3×3).

as prescribed by the theory. Such rubber hinges lead to the multistable states of the cell as they are able to store energy while folding. Finally, the unit cell was built by bonding together the panels and hinges (Fig. S7(D)). As the panels are characterized by different interior angles, different colored paper disks (10 mm in diameter) were attached to their faces to interpret the unit cell's elements, as shown in Fig. S7(C). This helps also to visualize, at first glance, which panels are being activated during the snapping mechanism. The orange, green, red, and blue disks indicate, respectively, the panels with interior acute angles of 50 deg, 60 deg, 70 deg, and 60 deg. A drawback of using rubber and Polypropylene components is their quite difficulty bonding. Specific instant adhesives were used to circumvent this problem. First, the rubber and Polypropylene surfaces were prepared with a Loctite SF 770® (by Henkel) primer. This product is specific to improve the adhesion of polyolefin

and low-energy surfaces. Then, both Polypropylene hinges and rubber hinges were bonded into the PC panel seats with the Loctite® 406 (by Henkel) and with Loctite® 4902 (by Henkel), respectively. The latter is a highly flexible cyanoacrylate adhesive designed to bond flexible components and prevent the stress cracking problem. Finally, each unit cell was jointed together by Polypropylene hinges to create the 1D assembly (Fig. S7(E)) and the 2D tessellation (Fig. S7(F)). The hinges used to join the unit cells were obtained by cutting a 0.5 mm thick white Polypropylene sheet (hinge type II in Fig. S7(C)). In this case, the hinges were bonded on the PC panels using the Loctite® 406 in combination with the Loctite® 770 primer.

B: Triclinc unit cell and 2D tessellation for the Poisson's ratio measurements

To capture shape-morphing, from the Eggbox mode to the Miura mode (and vice versa), of the 2D tessellation over time and give evidence of its reversible auxeticity, the tristable unit cell was modified as follows. *First, the rubber hinges were replaced with free hinges to avoid snapping behavior. This is essential to make the Poisson's ratio quantitative measurements reliable, repeatable (easy to be performed), and smooth over time. Second, the unit cell is not the assembly of panels and hinges bonded together but consists of a single piece of Polypropylene folded from its flat configuration and closed with just one bond.* Such a piece was obtained by milling a 1 mm thick Polypropylene sheet, the same used to realize the free hinges of the tristable cell, with the Roland EGX-600 CNC 3-axes engraving machine (Fig. S8(A)). The folding lines, namely the free hinges, were milled directly on the flat sheet before folding by a ball end mill (radius 1 mm) mounted on the milling machine. A stack of unit cells before their folding and boding are shown in Fig. S8(B). The panels and hinges were designed to mimic as much as possible the ideal unit cell investigated theoretically characterised by the geometrical parameters $a = c = 40$ mm and $\alpha = 60°$ and $\delta = 10°$.

The unit cell was designed to be modular and to permit an easy assembly of the 2D tessellation. To achieve the goal, each unit cell was realized with 2 seats and 2 extensions to allow a perfect glued male-female union, as shown in Fig. S8(C). Finally, the 4×7 2D tessellation was generated by joining together 28 unit cells using the Loctite® 406 in combination with the Loctite® 770 primer. The 2D tessellation used to perform the Poisson's ratio experiments is depicted in Fig. S8(D).

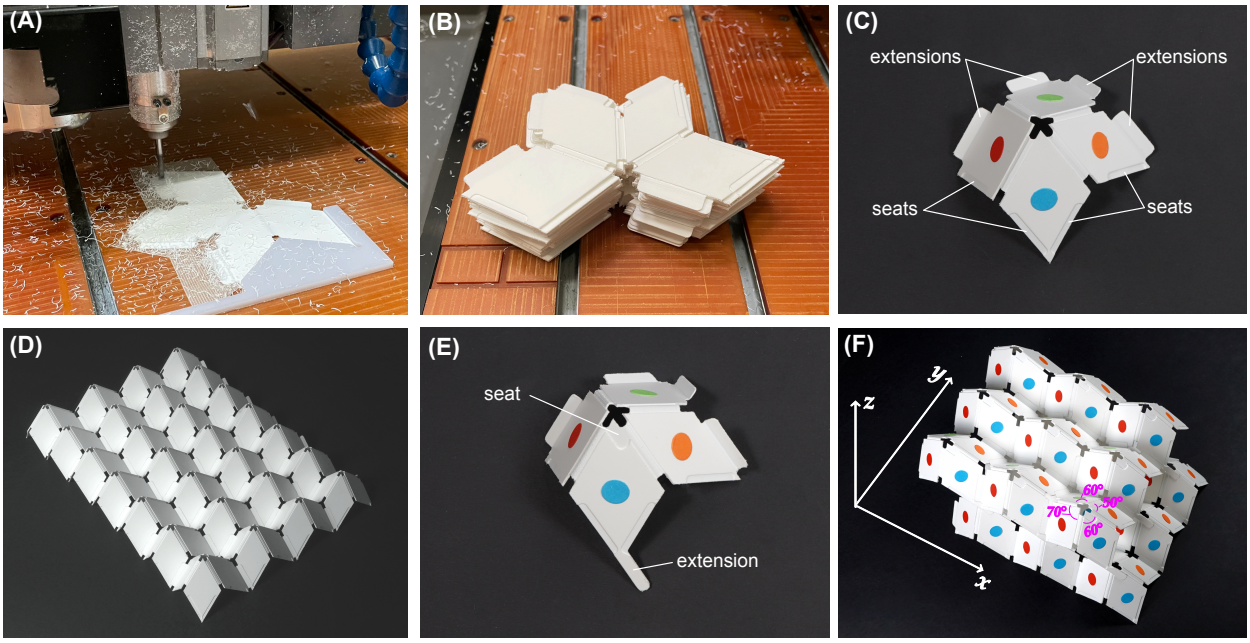

Fig. S8. (A) Engraving machine in action. A 1 mm thick Polypropylene sheet is milled to create the unit cell used to perform the Poisson's ratio measurements. The folding lines, namely the free hinges, were milled directly on the flat sheet before folding. (B) Stack of unit cells before the assembly. (C) Assembled unit cell. The figure emphasizes the modular nature of the designed element: 2 seats and 2 extensions are created to allow a fully glued male-female union between different unit cells. (D) Photo of the 2D (7×4) tessellation exploited to perform the quantitative tensile/compression experiments. (E) Unit cell specifically designed to merge several 2D tessellations on more levels. (F) 3D (3×3×2) metamaterials obtained by the union of 2 levels of 2D tessellations. The colored paper disks (10 mm in diameter) indicate the unit cell elements with acute interior angles of 50 deg (orange), 60 deg (green and blue), and 70 deg (red).

C: 3D metamaterial

The unit cell used for the Poisson's ratio measurements was slightly modified to permit the assembly in the z direction and thus to create the 3D metamaterial. A specific seat and extension was introduced on the panel characterized by interior acute angles of $\alpha = 60°$. The detail of such a modification is reported in Fig. S8(E). This trick enables, by a glued male-female union, to vertically merge several 2D tessellations on more levels, as shown Fig. S8(F). Different colored paper disks (10 mm in diameter) were attached to the faces of the panels to interpret the unit cell's elements. The choice of the colors is consistent with those

adopted for the tristable unit cell (orange 50 deg, red 70 deg, blue and green 60 deg).

VII: Origami Experiments

A: Snapping Experiments

Qualitative experiments were performed to give evidence of the multistable states of the unit cell, the 1D assembly, and the 2D tessellation. The snapping between each stable configuration was induced by a force applied by hand to the panels being activated. A movie showing the change of stable states is provided as Movie S2. In the movie, a *click sound* identifies the change of stable state when moving between different configurations.

B: Tessellation Experiments

Quantitative experiments were performed to verify the reversible auxetic behavior of the origami-based 2D metamaterial. The experiments were performed by using two different setups, called *basic setup* and *Saint-Venant setup*. Both setups were designed to perform the tension/compression tests on the 2D tessellation and to monitor its transversal (y direction) and longitudinal (x direction) displacements. All the experiments were recorded with a 4K Sony PXW-FS5 video camera (3840 $\times$ 2160 pixels, 24 fps), and the pictures were taken by a Sony Alpha 9 camera.

1: Saint Venant setup

This noteworthy experimental campaign on the Trimorph pattern was performed using the special setup shown in Fig. S9, namely the *Saint-Venant setup*. The fixture system of the *basic setup* has been redesigned to permit an almost perfect uniform transverse deformation during uniaxial testing, thus eliminating Saint-Venant end effects in the constrained region of the tessellation. This novel gripping mechanism permits to replicate, in a real experiment, the boundary conditions underlying the theoretical analysis. The fixture consists of a slide rail system (purchased from MiSUMi Europe) made up of several sliders inserted into a rail, as shown in S9A, B. Each slider comprises a rolling bearing system to reduce the friction with the rail. The rail was, in turn, connected to the testing machine by two aluminum

profiles. Due to the particular folding mechanism of the Trimorph pattern, five and four sliders were used to connect, respectively, the right and the left short side of the tessellation.

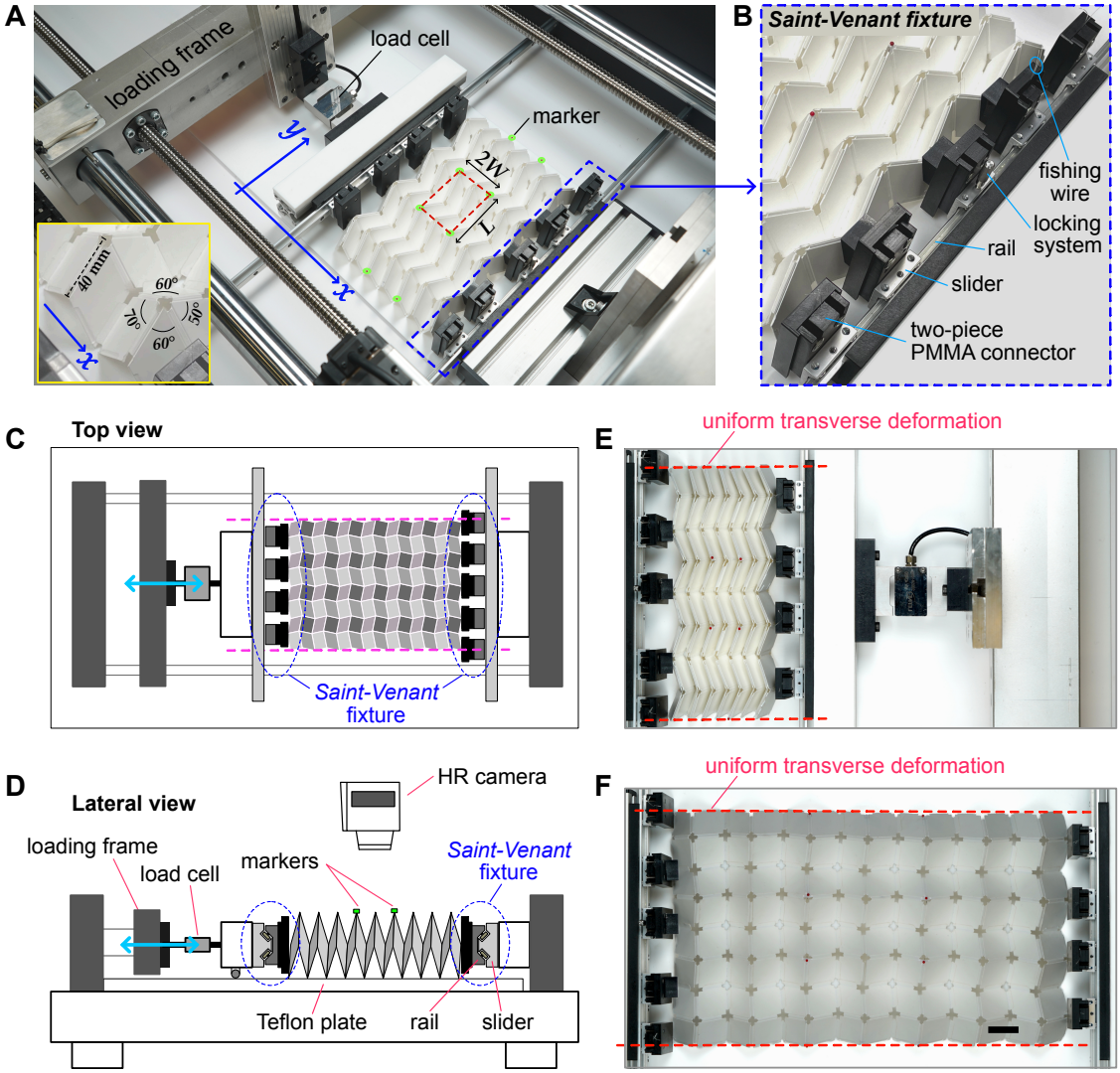

Fig. S9. (**A**) Photo of the experimental setup used to perform the tensile/compression test and verify the reversible auxeticity of the 2D tessellation by the use of the novel *Saint Venant fixture*. (**B**) Detail of the *Saint-Venant fixture*. (**C**) Schematic top and (**D**) lateral view of the testing platform showing the position of the 4K camera used to record the experiments. (**E-F**) Snapshots taken during the execution of the test showing an almost perfect uniform transverse deformation during the folding/unfolding process. Scale bar: 20 mm.

A two-piece PMMA connector is interposed between the aluminium slider and the tessellation to facilitate the punctual connection of the tessellation with the slider and allowing the

fine-tuning of the vertical position of the connecting point. A fishing wire (0.65 mm in diameter) has been used to connect the panels to the PMMA connector. The wire was carefully tensioned to keep the panels perfectly connected to the PMMA connector during the whole folding/unfolding process. To prevent rigid motion of the tessellation, one slider (in the middle) was fixed through a locking mechanism on the rail (S9B). The tension/compression experiments were performed by a MIDI 10 loading machine (by Messphysik, 0.05 μm stroke measurement resolution) turned horizontally to avoid out-of-plane bucking of the sample during the tests and gravitational effect. A low-friction Teflon plate was used to support the tessellation during the tests. The unixaial testing were performed by imposing a constant speed of 1.5 mm/s at one end of the sample as in the first experimental campaign. In particular, a higher speed would have effected the measurements with spurious inertia contribution. During the execution of the tests, the applied load was acquired with a DBSSM-1kg (by Leane International) load cell and the displacement with a transducer mounted internally to the testing machine. The measured displacement correspond to the evolution of total length of the tessellation during the folding/unfolding process. The experimental data were recorded with a Ni-cDaq 9188 acquisition system interfaced with a PC through a code developed in LabVIEW 2020. Four red spherical markers (1 mm in diameter), located along the sides of a rectangular region in the middle of the sample (Fig. S9A), were used to determine the Poisson's ratio of the tessellation. The displacements of each marker were determined by a post-processing analysis of the records of the experiments taken with a 4K Sony PXW-FS5 video camera (3840 $\times$ 2160 pixels, 24 fps) and positioned orthogonally to the testing platform, as sketched in Fig. S9D. The *Saint-Venant fixture* allows for a completely free sample deployment by eliminating the dog-bone shape that has a negative impact on the measurement of Poisson's ratio (Fig. S9E-F).

2: Basic Setup

This experimental campaign was performed using the setup shown in Fig. S10, namely with the *basic setup*. The whole apparatus was arranged horizontally to prevent the gravitational effect and reduce the out-of-plane instability during the compression tests. The tessellation was placed on a Teflon plate to reduce the friction with the experimental support. The two short sides of the tessellation were fixed with a fishing wire to two aluminium

profiles. This constraint was realized in a way to prevent the relative longitudinal displacements between the tessellation and the profiles but leaving sufficiently free those transverse displacements. One aluminium profile is fixed on the optical table while the other is at-

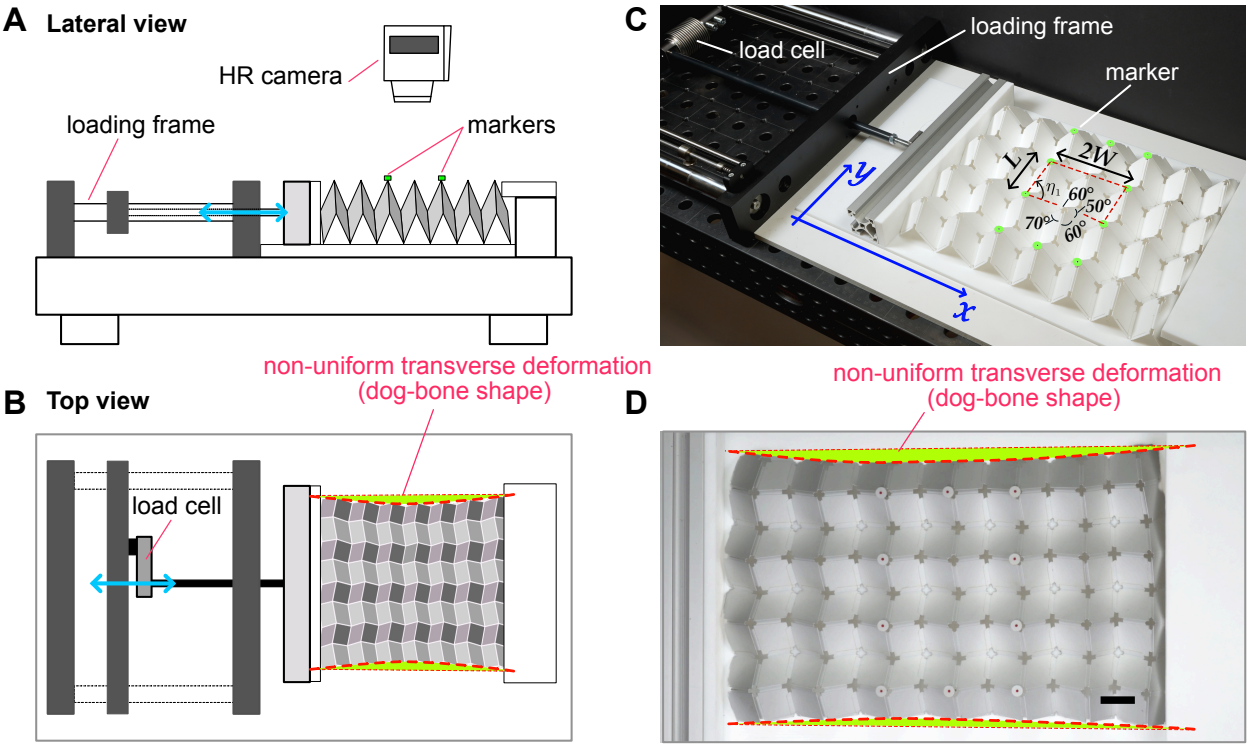

Fig. S10. Schematics of the lateral (A) and top (B) view of the experimental setup showing the position of the 4K camera used to record the experiments. (C) Photo of the *basic setup* used to perform the tensile/compression test and verify the reversible auxeticity of the 2D tessellation. (D) Snapshot taken during the execution of the test showing the non-uniform transverse deformation (dog-bone shape highlighted in green) caused by the constraints at the end of the sample, which reduces the accuracy of the experimental measurements and resulting Poisson's ratio. Scale bar: 20 mm.

tached via a metal stinger (650 mm in length) to the testing machine used to apply the longitudinal displacement to the sample. The sides of the aluminium profiles in contact with the tessellation were coated with a Teflon sheet. This expedient was adopted to reduce friction and leave as free as possible the transversal movements of the sample during the tests. The experiments were carried out by imposing a constant speed of 1.5 mm/s at one end of the sample with a μ-strain testing machine (resolution of the stroke measurement is 0.1 μm, by Messphysik). Such a speed was carefully chosen, combining the need to ensure

the quasi-static condition and the requirement to reduce the stick and slip phenomena between the sample and the testing Teflon platform. In particular, a higher speed would have effected the measurements with spurious inertia contribution. Four black markers (1 mm in diameter), located along the sides of a rectangular region in the middle of the sample (Fig. S10A,C), were used to determine the Poisson's ratio of the tessellation. The displacements of each marker were determined by a post-processing analysis of the records of the experiments taken with a 4K Sony PXW-FS5 video camera (3840 $\times$ 2160 pixels, 24 fps) and positioned orthogonally to the testing platform, as sketched in Fig. S10(A).

3: Tracking analysis

A *digital image correlation (DIC) and tracking method* was used to estimate the displacement field of the markers. The location of the markers was chosen to reduce the local effects of constraints on the experimental results. Such an approach was essential using the *basic setup*. The color of the markers was selected to enhance color contrast with the origami pattern to be tested. Such a choice facilitate the motion capture of the markers over time by a *digital image correlation and tracking method*. The technique involves several steps. First, the movies of the experiments were recorded at 24 fps with a 4K Sony PXW-FS5 video camera synchronized with the testing machine and placed orthogonal to the testing platform. The camera was equipped with a telephoto G Master FE 100-400 mm lens to reduce distortion and create contrast between the foreground and background. Then, the visibility of the tracking markers was enhanced by transforming the colored frames to their green (background) and black (markers) versions. After this process, each snapshot appears green everywhere except for the black markers. Finally, a frame-by-frame tracking analysis was performed on the enhanced frames by an *in-house* code developed in Mathematica. Such a code allows capturing the evolution of the coordinates of the centre of mass of each marker. Since the experiments are quasi-static, only 0.8 fps were considered to estimate the Poisson's ratio.

4: Discussion of experimental results

The comparison between theory and experiments, performed using the *Saint-Venant setup* and the *basic setup*, are reported in Fig. S11 and in Fig. S12, respectively. In the figures, the experiments are shown by different markers while the theoretical prediction by the black lines. In the latter case, the dashed line refers to the Eggbox mode, while the continuous line refers to the Miura mode Type II. The forward difference scheme was adopted to compute the Poisson's ratio note the displacements of the markers for each considered frame. In particular, the Poisson's ratio ν_i, associated to the generic frame i, was computed via the relation

$$\nu_i = -\frac{W_i}{L_i}\frac{L_{i+1} - L_i}{W_{i+1} - W_i}, \tag{S53}$$

where W and L are the width and the length of the unit cell, respectively. Such values were estimated by averaging the longitudinal and transverse displacements of markers located along a rectangular region in the middle of the tessellation. A two-points moving average was applied to slightly smooth the data obtained from Eq. S53 and to produce the graph of Fig. S11 and of Fig. S12 of the main text. This expedient was needed to eliminate spurious effects from the experimental data that inevitably arise during the execution of the tests. Such effects are mainly due to i) the sample and markers adjustments, ii) friction and stick and slip phenomena between the bottom side of the tessellation and the Teflon sheet.

a: Experiments using the Saint-Venant setup In each graph of Fig. S11, three different experiments (shown with different markers) are superimposed to the theoretical prediction. In the figure, the left column refers to the tension experiments, while the right column to the compression experiments. The Poisson's ratio measurements are shown in Figs. S11A and B. The comparison between the measured shear-coupling coefficient and the theory is shown in Figs. S11C (tension) and D (compression). Finally, in Figs. S11E and F, the load-displacement data recorded during the execution of the tests are superimposed to the analytical formula (see section II D). The displacement is defined as the total extension of the entire sample, while the load is measured at the side of the sample connected to the movable cross-head of the testing machine, as illustrated in the insets of Figs. S11E and F. A movie showing reversible auxeticity of the 2D tessellation over time and the comparison between theory and experimental results obtained with the *Saint-Venant setup* is provided as

Movie S1. To evaluate the theoretical formulae (Poisson Ratio's, Shear-Coupling coefficient,

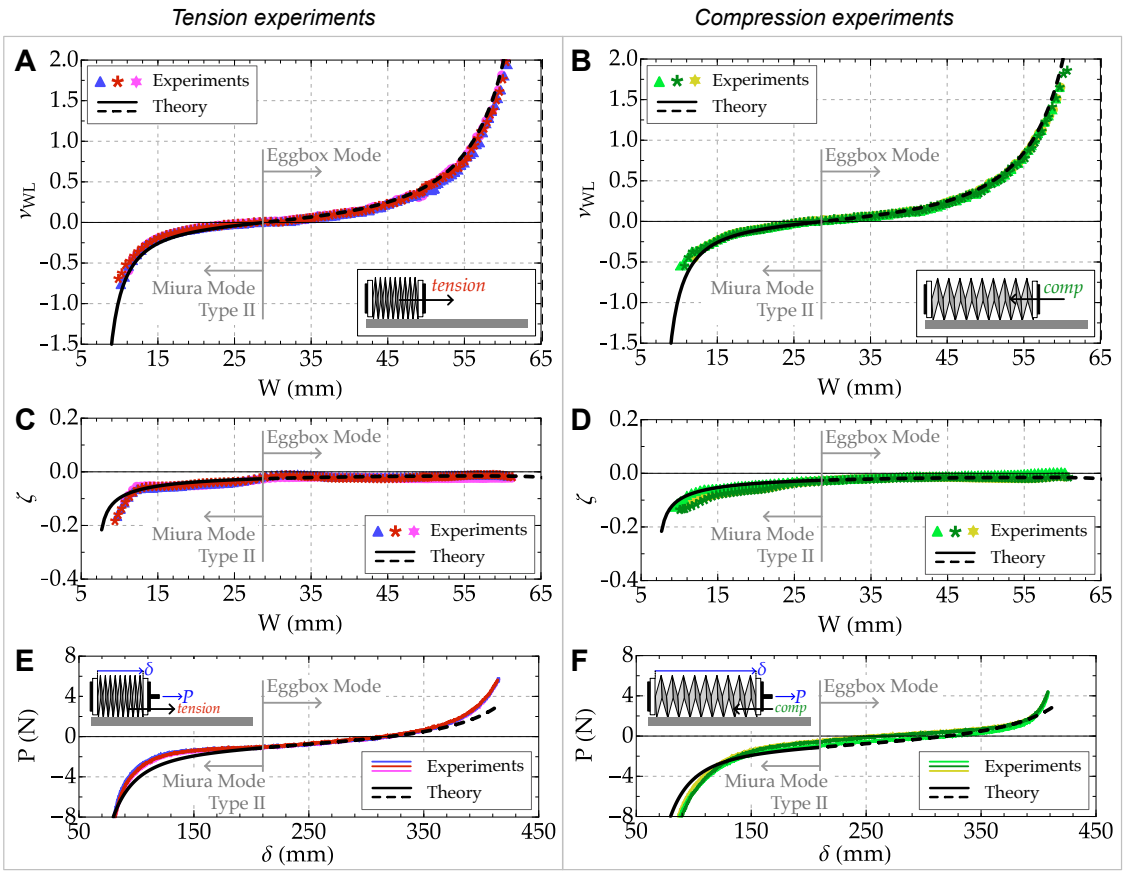

FIG. S11. Geometric mechanics of the Trimorph origami-based assembly (2D) using the *Saint Venant setup*. (**A-B**) The lattice Poisson's ratio ν_{WL} vs. average unit cell length W, measured in tension and compression tests, respectively. The same sample is tested three times, and the results are shown by different markers. (**C-D**) The shear-normal coupling coefficient ζ vs. average unit cell length W. (**E-F**) Load-displacement diagram. The displacement is defined as the total extension of the entire sample, as illustrated in the insets.

Load vs. Displacement) in predicting the observed data, we have computed the coefficient of determination R^2 for all the experiments reported in Fig. 5. Such a coefficient is defined as:

$$R^2 = 1 - \frac{SS_{res}}{SS_{tot}}, \tag{S54}$$

where SS_{res} represents the sum of the squares of the residual errors ($SS_{res} = \sum_i (y_i - y_{th})^2$) and SS_{tot} is the total sum of squares associated with the outcome variable, defined as the sum of the squares of the measurements minus their mean ($SS_{tot} = \sum_i^N (y_i - \bar{y})^2$). In the

previous formulae, y_i represents each experimental data points, y_{th} the corresponding value predicted by the theoretical formulae, and $\bar{y}$ the mean value of the experimental data over the range of interest ($\bar{y} = 1/n \sum_i^N y_i$).

It is evident from its definition that the higher is the agreement between the experimental data and the theory, the more the coefficient of determination R^2 is close to 1. An $R^2 = 1$ would represent the limit case of a perfect agreement between the theory and the experiments.

We have evaluated the mean coefficient of determination R^2 and its standard deviation for both the tension tests and the compression tests, taking into account all the performed experiments (three in tension and three in compression).
In the case of the Poisson's ratio tests, we have observed a coefficient of determination $R^2 = 0.984 \pm 0.007$ and $R^2 = 0.982 \pm 0.003$, for the tension and compression experiments, respectively. Such values are very close to 1 , thus meaning that the theory and the experiments are in very well agreement.

For the Shear-normal coupling coefficient we have observed a coefficient of determination $R^2 = 0.812 \pm 0.059$ and $R^2 = 0.78 \pm 0.070$, for the tension and compression experiments, respectively. In this case a value slightly lower than 1 is observed, mainly caused by the panel thickness when extreme folding is achieved.

For the Load vs. Displacement a coefficient of determination $R^2 = 0.90 \pm 0.021$ and $R^2 = 0.92 \pm 0.020$, has been observed in tension and compression, respectively. Also in this case a value slightly lower than 1 is observed, but, overall the agreement is reasonably good.

b: Experiments using the Basic setup The Poisson's ratio and the shear-normal coupling coefficient as a function of the cell with W are reported in Fig. S12A, C for the tension experiment, and in Fig. S12B, D for the compression experiment. In the figures, the markers represent the experimental results obtained from a tensile test (magenta/stars) and a compression test (green/disks). A slight perturbation of the measured Poisson's ratio is observed during the tensile test for a width W of about 43.4 mm. An in-depth analysis of the W versus L graph of Fig. S12E shows clearly that such disturbance is associated with the previously mentioned practical problems. Although the L versus W curve is very smooth at first glance, the zoom of the region near 43.4 mm shows a bit of *noise* in the experimental data. This abrupt fluctuations compromise the derivative of Eq. S53 leading to the artificial spikes in the calculated values of ν_i. The results reported in Fig. S12 show a

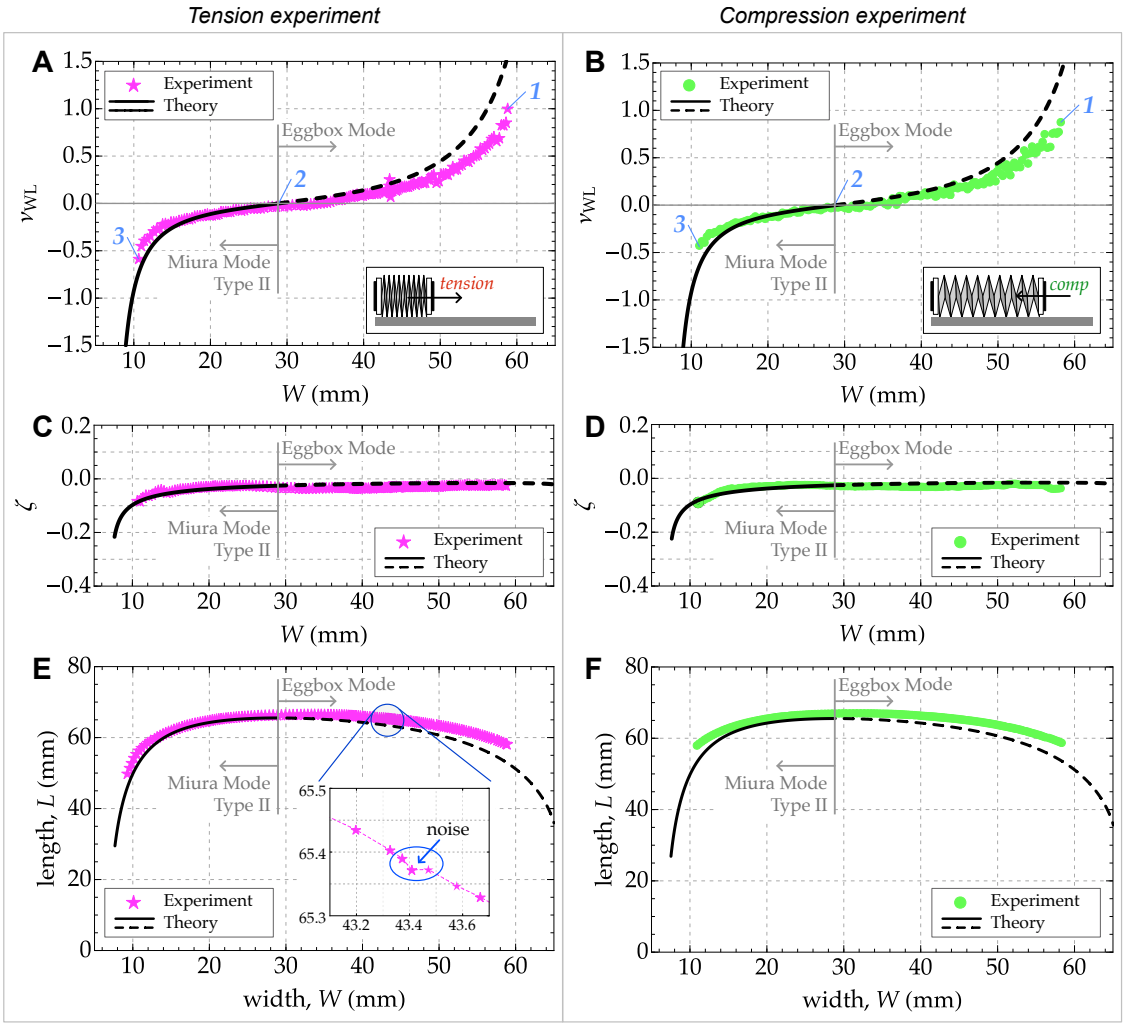

FIG. S12. Geometric mechanics of the Trimorph origami based metamaterial (2D) using the *Basic setup*. The Lattice Poisson Ratio ν_{WL} vs. average unit cell length W observed in tension (**A**) and compression (**B**). The numbers 1, 2, and 3 in the graph correspond to the snapshots reported in Fig. S13A and B. The shear-normal coupling coefficient ζ vs. average unit cell length W observed in tension (**A**) and compression (**B**). Relation between the width W and the length L of the unit cell observed during a tension (**E**) and compression (**F**) test. The inset of sub-figure **E** provides the explanation of the noise in the experimental data of the Poisson's ratio (sub-figure **A**) attained for a width W of about 43.4 mm during a tension test.

globally good agreement between theory and both tensile and compression tests throughout the W range between 10 mm and 58 mm. The experimental results reported in the figure provide a full display of reversible auxeticity for a Poisson's ratio that switches from -0.6 to +1. In the figure, the labels 1, 2, 3 refer to the sequence of photos reported in Fig. S13A and

B documenting the folding/unfolding mechanisms of the 2D tessellation. The snapshots of Fig. S13A refer to the unfolding mechanism, namely associated to a tensile test, while those of Fig. S13B refer to the folding mechanism, namely associated to a compression test. The

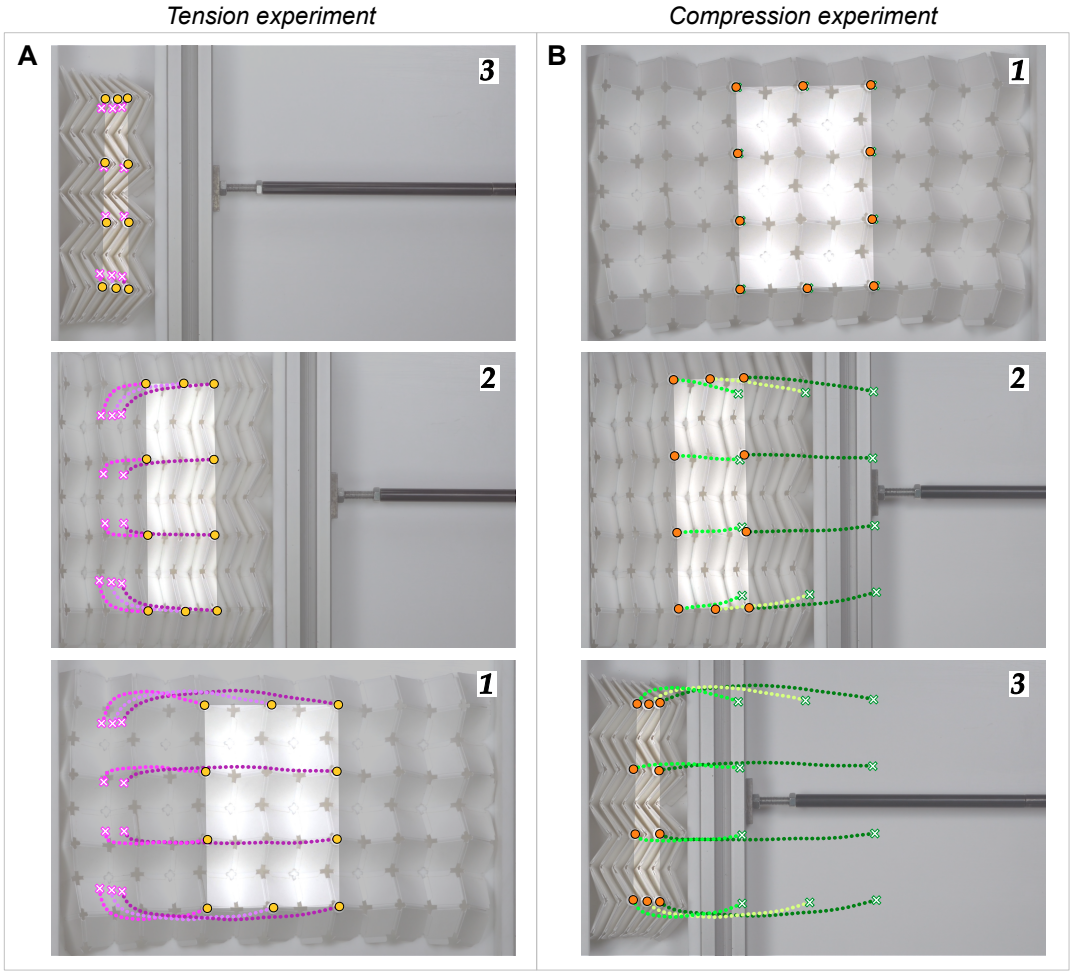

FIG. S13. (**A**) Snapshots taken during the tension test. (**B**) Snapshots taken during the compression test. The dashed lines indicates the trajectories of the markers.

path followed by each markers to move from the initial configuration to the current configuration is superimposed to each snapshot with green/dashed lines (compression) and with magenta/dashed lines (tension). Such trajectories, being the evolution of the coordinates of the markers over time, were obtained from the tracking analysis exploited to estimate the Poisson's ratio. The shape of the trajectories highlighted in the snapshots provides a visual interpretation of the continuous morphing of the unit cells composing the tessellation between a Miura mode and an Eggbox mode. The point of maximum enlargement of the trajectories coincides with the Poisson's ratio switch from positive to negative, namely the

transition between Miura mode and an Eggbox mode (snapshots 2 in Figs. S13A and B). A movie showing the reversible auxeticity of the 2D tessellation over the time and the comparison between theory and experimental results obtained with the *basic setup* is provided as Movie S4.

VIII: MERLIN code (MATLAB) for numerical simulations

A: MATLAB function for defining Trimorph geometry

```
function [NODE,PANEL] = ...
ConfigTrimorph(x_divs,y_divs,a,b,c,d,alfa1,alfa2,alfa3,alfa4,v3i)
alfa1 = alfa1*pi/180; alfa2 = alfa2*pi/180;
alfa3 = alfa3*pi/180; alfa4 = alfa4*pi/180;
v3i = v3i*pi/180;
numx = 2*x_divs; numy = 2*y_divs;
[vs,asst] = Trimorph_Vertex(alfa1,alfa2,alfa3,alfa4,v3i);
psi = asst(1); phi = asst(2);
% v4p = asst(3); v4pp = asst(4);
L = sqrt(c^2+d^2-2*c*d*cos(phi));
W = sqrt(a^2+b^2-2*a*b*cos(psi));
sin_aW = b*sin(psi)/W; cos_aW = sqrt(1-sin_aW^2);
sin_cL = d*sin(phi)/L; cos_cL = sqrt(1-sin_cL^2);
cos_Wac = (-cos(alfa4)+cos(alfa1)*cos(psi))/(sin(alfa1)*sin(psi));
cos_acL = (-cos(alfa2)+cos(alfa1)*cos(phi))/(sin(alfa1)*sin(phi));
cos_cW = cos(alfa1)*cos_aW+sin(alfa1)*sin_aW*cos_Wac;
sin_acW = sin_aW*sqrt(1-cos_Wac^2)/sqrt(1-cos_cW^2);
cos_WcL = cos_acL*sqrt(1-sin_acW^2)+sqrt(1-cos_acL^2)*sin_acW;
cos_aL = cos(alfa1)*cos_cL+sin(alfa1)*sin_cL*cos_acL;
cos_LW = cos_cW*cos_cL+sqrt(1-cos_cW^2)*sin_cL*cos_WcL;
sin_LW = sqrt(1-cos_LW^2);

cos_WLc = (cos_cW-cos_cL*cos_LW)/(sin_cL*sin_LW);
h5p = c*d*sin(phi)/L;
h5 = h5p*sqrt(1-cos_WLc^2);
dlt5 = h5p*cos_WLc;

cos_aWL = (cos_aL-cos_aW*cos_LW)/(sin_aW*sin_LW);
h8p = a*b*sin(psi)/W;
h8 = h8p*sqrt(1-cos_aWL^2);
dlt8 = h8p*cos_aWL;

[X,Y] = meshgrid(linspace(0,L/2*numx,numx+1),linspace(0,W/2*sin_LW*numy,numy+1));
Z = 0*X;
X(3:2:end,1:2:end) = X(3:2:end,1:2:end)+...
repmat([W*cos_LW:W*cos_LW:W*cos_LW*y_divs]',1,x_divs+1);
X(1:2:end,2:2:end) = X(1:2:end,1:2:end-1)+sqrt(c^2-h5p^2);
Y(1:2:end,2:2:end) = Y(1:2:end,1:2:end-1)+dlt5;
Z(1:2:end,2:2:end) = h5;
X(2:2:end,1:2:end) = X(1:2:end-1,1:2:end)+sqrt(a^2-h8p^2)*cos_LW+dlt8*sin_LW;
Y(2:2:end,1:2:end) = Y(1:2:end-1,1:2:end)+sqrt(a^2-h8p^2)*sin_LW-dlt8*cos_LW;
```

```
Z(2:2:end,1:2:end) = h8;
X(2:2:end,2:2:end) = X(2:2:end,1:2:end-1)+sqrt(c^2-h5p^2);
Y(2:2:end,2:2:end) = Y(2:2:end,1:2:end-1)+dlt5;
Z(2:2:end,2:2:end) = h5+h8;
NODE = [reshape(X,[],1),reshape(Y,[],1),reshape(Z,[],1)];

k = 0; PANEL = cell(numx*numy,1);
for j=1:numy, for i=1:numx
k = k+1;
n1 = (i-1)*(numy+1)+j; n2 = i*(numy+1)+j;
PANEL{k} = [n1 n2 n2+1 n1+1];
end, end

function [vs,asst] = Trimorph_Vertex(alfa1,alfa2,alfa3,alfa4,v3i)
% alfa1 >= alfa2 >= alfa4 >= alfa3
tol = 1e-10;
havpsi = sin((alfa2-alfa3)/2)^2+sin(alfa2)*sin(alfa3)*sin(v3i/2)^2;
psi = asin(sqrt(havpsi))*2;
havv1 = (havpsi-sin((alfa1-alfa4)/2)^2)/(sin(alfa1)*sin(alfa4));
v1 = real(asin(sqrt(havv1)))*2;
v4p = real(asin(sin(v1)*sin(alfa1)/sin(psi)));
if abs(cos(alfa1)-(cos(psi)*cos(alfa4)+sin(psi)*sin(alfa4)*cos(pi-v4p)))<tol
v4p = pi-v4p;
end
if v3i>pi, sgn=-1; else, sgn=1; end
v4pp = real(asin(sgn*sin(v3i)*sin(alfa2)/sin(psi)));
if abs(cos(alfa2)-(cos(psi)*cos(alfa3)+sin(psi)*sin(alfa3)*cos(pi-v4pp)))<tol
v4pp = pi-v4pp;
end
v4 = v4p+sgn*v4pp;
havphi = sin((alfa3-alfa4)/2)^2+sin(alfa3)*sin(alfa4)*sin(v4/2)^2;
havv2 = (havphi-sin((alfa1-alfa2)/2)^2)/(sin(alfa1)*sin(alfa2));
v2 = real(asin(sqrt(havv2)))*2;
if nargout < 2
vs = [v1;v2;v3i;v4];
else
vs = [v1;v2;v3i;v4];
phi = asin(sqrt(havphi))*2;
asst = [psi;phi;v4p;v4pp];
end
```

B: MATLAB function for finding rest angles

```
function [RestAngles, LocalMinima] = TristableDesign(alpha, delta)
Cgamma3=(cot(alpha)*sin(alpha-delta)-csc(alpha)*sin(delta)-1)/(cos(alpha-delta)+1);
Cgamma1=(Cgamma3*sin(alpha-delta)+2*cos(alpha)*sin(delta))/(sin(alpha+delta));
gammastar=acos(Cgamma1);

x0=[gammastar/2; 0.0];
options = optimoptions('fsolve','Display','iter');
[xopt,~] = fsolve(@(x)tangentpoints(x,alpha,delta,gammastar),x0,options);

[~, centr] = tangentpoints(xopt,alpha,delta,gammastar);
RestAngles = [centr, centr];
LocalMinima = [gammastar,gammastar; xopt(1), xopt(2); xopt(2), xopt(1)];
end

function [F,centr]=tangentpoints(x,alpha,delta,gammastar)
f1 = -cos(alpha-delta) + (cos(alpha))^2*cos(alpha+delta) -...
cos(alpha+delta)*(sin(alpha))^2*cos(x(1))*cos(x(2))+...
(sin(alpha))^2*sin(x(1))*sin(x(2))+...
cos(alpha)*sin(alpha)*sin(alpha+delta)*(cos(x(1))+cos(x(2)));
k=(cos(x(2))*(sin(alpha))^2*sin(x(1)) + ...
cos(x(1))*cos(alpha+delta)*(sin(alpha))^2*sin(x(2))-...
cos(alpha)*sin(alpha)*sin(x(2))*sin(alpha+delta))/...
(cos(x(2))*cos(alpha+delta)*(sin(alpha))^2*sin(x(1))+...
cos(x(1))*(sin(alpha))^2*sin(x(2))-cos(alpha)*sin(alpha)*sin(x(1))*sin(alpha+delta));
centr=(k*x(1)-x(2))/(k-1);
F=[f1;x(1)^2+x(2)^2-2*(x(1)+x(2))*centr-2*gammastar^2+4*gammastar*centr];
end
```

C: MERLIN script for single unit cell simulation

```
%% =========== TRIMORPH UNIT CELL ===================================== %%
clear all; close all; clc;
%% Define geomtry
x_divs = 1; y_divs = 1;
a = 10; b = 10; c = 10; d = 10;
alfa1 = 70; alfa2 = 60; alfa3 = 50; alfa4 = 60; dlta = (alfa1-alfa2);
gmma3 = acos((cot(alfa2/180*pi)*sin(alfa3/180*pi)-...
csc(alfa2/180*pi)*sin(dlta/180*pi)-1)/(cos(alfa3/180*pi)+1))/pi*180;
[Node,Panel] = ConfigTrimorph(x_divs,y_divs,a,b,c,d,alfa1,alfa2,alfa3,alfa4,gmma3);

[RestAngles, LocalMinima] = TristableDesign(alfa2/180*pi, (alfa1-alfa2)/180*pi);

% Visualize initial configuration
figure()
PlotOri(Node,Panel,[],'ShowNumber','on');
axis equal

%% Set up boundary conditions
Supp = [ 1, 1, 0, 1;
3, 1, 0, 1;
2, 0, 1, 0;
7, 0, 0, 1;
9, 0, 0, 1;
8, 0, 1, 0];

Load = [8, -1, 0, 0];
indp = Load(:,1);

%% Define material and modeling parameters
% Simulation options using the N5B8 model
AnalyInputOpt = struct(...
'ModelType','N5B8',...
'MaterCalib','auto',...
'ModElastic', 2e2,...
'Poisson', 0.3,...
'Thickness', 0.5,...
'Kf', 0.01, ...
'Kb', 0.1, ...
'RotSprBend', @(he,h0,Kb,L0)EnhancedLinear(he,h0,Kb,L0,15,345),...
'RotSprFold', @(he,h0,Kf,L0)EnhancedLinear(he,h0,Kf,L0,15,345),...
'LoadType','Force',...  % Force load
'InitialLoadFactor', 0.001,...
'MaxIcr', 70);
```

```
%% Perform analysis
% Assemble input data
[truss, angles, AnalyInputOpt] = PrepareData(Node,Panel,Supp,Load,AnalyInputOpt);
nfold = y_divs*2*(x_divs*2-1) + x_divs*2*(y_divs*2-1);
zerorotind = zeros(nfold/2,1);
% Find indices of all gamma_3, gamma_4 hinges,
% and interfaces between unit cells
m = 1;
for px = 1:x_divs
for py = 1:y_divs
ctr = (2*px-1)*(y_divs*2+1) + 2*py;
edge1 = sort([ctr,ctr+1],2);
[~,index_A,index_B] = intersect(angles.fold(:,1:2),edge1,'rows');
if ~isempty(index_A)
zerorotind(m) = index_A;
m = m+1;
end
edge2 = sort([ctr,ctr+(y_divs*2+1)],2);
[~,index_A,index_B] = intersect(angles.fold(:,1:2),edge2,'rows');
if ~isempty(index_A)
zerorotind(m) = index_A;
m = m+1;
end
edge3 = sort([ctr+1,ctr+(y_divs*2+2)],2);
[~,index_A,index_B] = intersect(angles.fold(:,1:2),edge3,'rows');
if ~isempty(index_A)
zerorotind(m) = index_A;
m = m+1;
end
edge4 = sort([ctr+(y_divs*2+1),ctr+(y_divs*2+2)],2);
[~,index_A,index_B] = intersect(angles.fold(:,1:2),edge4,'rows');
if ~isempty(index_A)
zerorotind(m) = index_A;
m = m+1;
end
end
end
fixrotind = setdiff(1:nfold,zerorotind);
% Assign almost zero stiffness
angles.Kf(zerorotind) = 1e-10;
% Assign rest angles to gamma_1 and gamma_2 hinges
% i.e., \bar{\gamma_1} & \bar{\gamma_2}
for k = 1:numel(fixrotind)
if angles.pf0(fixrotind(k))<=pi
angles.pf0(fixrotind(k)) = RestAngles(1);
```

```
else
angles.pf0(fixrotind(k)) = 2*pi - RestAngles(1);
end
end

% Specify initial deformation state
truss.U0 = zeros(3*size(truss.Node,1),1);
% Perform path-following analysis
[Uhis,Fhis] = PathAnalysis(truss,angles,AnalyInputOpt);
% Postprocess output data
Uhis = real(Uhis);
Fhis = real(Fhis);
STAT = PostProcess(Uhis,truss,angles);

%% Visualize simulation
instdof = [indp(1),-1]; % [Nodal index, Direction]
interv = 1; endicrm = size(Uhis,2);
% Animation monitoring node-wise change
VIntensityDataInten = zeros(size(truss.Node,1),size(Uhis,2));
IntensityDataM = bsxfun(@times,STAT.bar.Sx,truss.A);
for k = 1:size(Uhis,2)
IntensityDataIntenk = sparse(truss.Bars(:,1),truss.Bars(:,2),...
abs(IntensityDataM(:,k)),size(truss.Node,1),size(truss.Node,1));
VIntensityDataInten(:,k) = sum((IntensityDataIntenk+IntensityDataIntenk'),2);
end
VisualFold(Uhis(:,1:interv:endicrm),truss,angles,Fhis(1:interv:endicrm,:),...
instdof,'IntensityMap','Vertex','IntensityData',VIntensityDataInten)

%% Plot diagrams
% Plot load vs displacement
dsp = sign(instdof(2))*Uhis((instdof(1)*3-(3-abs(instdof(2)))),:);
figure()
plot(dsp/a,Fhis/angles.Kf(1),'b-','linewidth',1);
axis tight
xlabel('Displacement','fontsize',14);
ylabel('Load','fontsize',14);

% Plot stored energy vs displacement
figure()
% Red line is the total energy.
plot(dsp/a,STAT.PE/angles.Kf(1),'r-','linewidth',2);
hold on
% Between red and cyan is the folding energy.
plot(dsp/a,STAT.bend.UB+STAT.bar.US/angles.Kf(1),'c-');
% Between cyan and magenta is the portion of energy for bending.
plot(dsp/a,STAT.bar.US/angles.Kf(1),'m-');
```

```
% Below magenta is the stretching energy of bars.
axis tight
xlabel('Displacement','fontsize',14);
ylabel('Stored Energy','fontsize',14);
```

D: MERLIN script for 2D tessellation simulation

```
%% =========== TRIMORPH TESSELLATION ================================== %%
clear all; close all; clc;
%% Define geomtry
x_divs = 5; y_divs = 5;
a = 10; b = 10; c = 10; d = 10;
alfa1 = 70; alfa2 = 60; alfa3 = 50; alfa4 = 60; dlta = (alfa1-alfa2);
[RestAngles, LocalMinima] = TristableDesign(alfa2/180*pi, dlta/180*pi);
gmma3 = acos((cot(alfa2/180*pi)*sin(alfa3/180*pi)-...
    csc(alfa2/180*pi)*sin(dlta/180*pi)-1)/(cos(alfa3/180*pi)+1))/pi*180;
[Node,Panel] = ...
    ConfigTrimorph(x_divs,y_divs,a,b,c,d,alfa1,alfa2,alfa3,alfa4,gmma3);

% Visualize initial configuration
% figure()
% PlotOri(Node,Panel,[],'ShowNumber','on');
% axis equal

%% Set up boundary conditions
defectpt = 61;
basept = defectpt - (y_divs*2+1);
cencol = floor(defectpt/(y_divs*2+1));
cenrow = defectpt - cencol*(y_divs*2+1);
corner1 = 1;
corner2 = (y_divs*2+1);
corner3 = (y_divs*2+1)*x_divs*2+1;
corner4 = (y_divs*2+1)*(x_divs*2+1);

linesupp = (cencol-1)*(y_divs*2+1) + [1:2:(y_divs*2+1)]';
lineload = (cencol+1)*(y_divs*2+1) + [2:2:(y_divs*2+1)]';

orientsupp = defectpt - 1;
Supp = [corner1, 0, 0, 1;
        corner2, 0, 0, 1;
        corner3, 0, 0, 1;
        corner4, 0, 0, 1;
        basept-1, 1, 1, 1;
        basept, 1, 0, 0;
        orientsupp, 0, 1, 0];

Load = [lineload, -ones(y_divs,1), zeros(y_divs,1), zeros(y_divs,1);
        linesupp, ones(numel(linesupp),1), zeros(numel(linesupp),1), ...
        zeros(numel(linesupp),1)];
indp = Load(:,1);
```

```
%% Define material and modeling parameters
% Simulation options using the N5B8 model
AnalyInputOpt = struct(...
    'ModelType','N5B8',...
    'MaterCalib','auto',...
    'ModElastic', 2e2,...
    'Poisson', 0.35,...
    'Thickness', 0.5,...
    'Kf', 0.01, ...
    'Kb', 0.1, ...
    'RotSprBend', @(he,h0,Kb,L0)EnhancedLinear(he,h0,Kb,L0,90,270),...
    'RotSprFold', @(he,h0,Kf,L0)EnhancedLinear(he,h0,Kf,L0,90,270),...
    'LoadType','Force',...  % Force load
    'InitialLoadFactor', 0.002,...
    'MaxIcr', 92);

%% Perform analysis
% Assemble input data for transition from (1*) to (2*)
[truss, angles, AnalyInputOpt] = PrepareData(Node,Panel,Supp,Load,AnalyInputOpt);
nfold = y_divs*2*(x_divs*2-1) + x_divs*2*(y_divs*2-1);
nonzerorotind = zeros(x_divs*y_divs*2,1);
% Find indices of all gamma_3, gamma_4 hinges,
% and interfaces between unit cells
m = 1;
for px = 1:x_divs
    for py = 1:y_divs
        ctr = (2*px-1)*(y_divs*2+1) + 2*py;
        edge1 = sort([ctr,ctr-1],2);
        [~,index_A,index_B] = intersect(angles.fold(:,1:2),edge1,'rows');
        if ~isempty(index_A)
            nonzerorotind(m) = index_A;
            m = m+1;
        end
        edge2 = sort([ctr,ctr-(y_divs*2+1)],2);
        [~,index_A,index_B] = intersect(angles.fold(:,1:2),edge2,'rows');
        if ~isempty(index_A)
            nonzerorotind(m) = index_A;
            m = m+1;
        end
    end
end
fixrotind = nonzerorotind;
zerorotind = setdiff(1:nfold,nonzerorotind);
% Assign almost zero stiffness
angles.Kf(zerorotind) = 1e-10;
```

```
% Assign rest angles to gamma_1 and gamma_2 hinges
% i.e., \bar{\gamma_1} & \bar{\gamma_2}
for k = 1:numel(fixrotind)
    if angles.pf0(fixrotind(k))<=pi
        angles.pf0(fixrotind(k)) = RestAngles(1);
    else
        angles.pf0(fixrotind(k)) = 2*pi - RestAngles(1);
    end
end

% Specify initial deformation state
truss.U0 = zeros(3*size(truss.Node,1),1);
% Perform path-following analysis for transition from (1*) to (2*)
[Uhis,Fhis] = PathAnalysis(truss,angles,AnalyInputOpt);
% Postprocess output data
Uhis = real(Uhis);
Fhis = real(Fhis);
STAT = PostProcess(Uhis,truss,angles);

%% Visualize simulation: (1*) -> (2*)
instdof = [defectpt+(2*y_divs+1),-1]; % [Nodal index, Direction]
interv = 1; endicrm = size(Uhis,2);
% Animation monitoring node-wise change
VIntensityDataInten = zeros(size(truss.Node,1),size(Uhis,2));
IntensityDataM = bsxfun(@times,STAT.bar.Sx,truss.A);
for k = 1:size(Uhis,2)
    IntensityDataIntenk = sparse(truss.Bars(:,1),truss.Bars(:,2),...
        abs(IntensityDataM(:,k)),size(truss.Node,1),size(truss.Node,1));
    VIntensityDataInten(:,k) = sum((IntensityDataIntenk+IntensityDataIntenk'),2);
end
VisualFold(Uhis(:,1:interv:endicrm),truss,angles,Fhis(1:interv:endicrm,:),...
    instdof,'IntensityMap','Vertex','IntensityData',VIntensityDataInten,...
    'recordtype','video','filename','Trimorph5x5_1to2')

%% Plot diagrams
% Load vs displacement
dsp = sign(instdof(2))*Uhis((instdof(1)*3-(3-abs(instdof(2)))),:);
figure()
plot(dsp/a,Fhis/angles.Kf(10),'b-','linewidth',1);
grid on;
xlabel('Displacement','fontsize',14);
ylabel('Load','fontsize',14);

% Stored energy vs displacement
figure(55)
% Red line is the total energy.
```

```
plot(dsp/a,STAT.PE/angles.Kf(10),'r-','linewidth',2);
hold on
% Between red and cyan is the folding energy.
plot(dsp/a,(STAT.bend.UB+STAT.bar.US)/angles.Kf(10),'c-');
% Between cyan and magenta is the portion of energy for bending.
plot(dsp/a,STAT.bar.US/angles.Kf(10),'m-');
% Below magenta is the stretching energy of bars.
axis tight

%% Simulate transition from transition from (2*) to (3*)
% Change boundary conditions
lineload2 = [cenrow+(2*y_divs+2):2*(2*y_divs+1):(2*x_divs+1)*(2*y_divs+1)]';
linesupp2 = [cenrow-1:2*(2*y_divs+1):(2*x_divs+1)*(2*y_divs+1)]';

Load = [lineload2, zeros(y_divs,1), -ones(y_divs,1),  zeros(y_divs,1);
        linesupp2, zeros(numel(linesupp),1), ones(numel(linesupp),1), ...
        zeros(numel(linesupp),1)];
%% Perform Analysis
% Assemble input data for transition from (2*) to (3*)
[~, ~, AnalyInputOpt] = PrepareData(Node,Panel,Supp,Load,AnalyInputOpt);
% Re-initialize starting configuration (total Lagrangian formulation)
truss.U0 = Uhis(:,end);

AnalyInputOpt.MaxIcr = 92;
AnalyInputOpt.InitialLoadFactor = 0.001;

[Uhis2,Fhis2] = PathAnalysis(truss,angles,AnalyInputOpt);
% Postprocess output data
Uhis2 = real(Uhis2);
Fhis2 = real(Fhis2);
STAT2 = PostProcess(Uhis2,truss,angles);

instdof = [62,-2]; % [Nodal index, Direction]
interv = 1; endicrm = size(Uhis2,2);
% Animation monitoring node-wise change
VIntensityDataInten = zeros(size(truss.Node,1),size(Uhis2,2));
IntensityDataM = bsxfun(@times,STAT2.bar.Sx,truss.A);
for k = 1:size(Uhis2,2)
    IntensityDataIntenk = sparse(truss.Bars(:,1),truss.Bars(:,2),...
        abs(IntensityDataM(:,k)),size(truss.Node,1),size(truss.Node,1));
    VIntensityDataInten(:,k) = sum((IntensityDataIntenk+IntensityDataIntenk'),2);
end
VisualFold(Uhis2(:,1:interv:endicrm),truss,angles,Fhis2(1:interv:endicrm,:),...
    instdof,'IntensityMap','Vertex','IntensityData',VIntensityDataInten,...
    'recordtype','video','filename','Trimorph5x5_2to3')
```

```
%% Plot diagrams
% Load vs displacement
dsp2 = sign(instdof(2))*Uhis2((instdof(1)*3-(3-abs(instdof(2)))),:);
dsp2 = dsp2-min(dsp2);
figure()
plot(dsp2/a,Fhis2/angles.Kf(10),'b-','linewidth',1);
axis tight; grid on;
ylim([-0.5,3])
xlabel('Displacement','fontsize',14);
ylabel('Load','fontsize',14);

% Stored energy vs displacement
figure(55)
hold on
plot([max(dsp/a),max(dsp/a)],[0,max(STAT2.PE/angles.Kf(10))*1.05])
plot(max(dsp/a)+dsp2/a,STAT2.PE/angles.Kf(10),'r-','linewidth',2);
% Red line is the total energy.
plot(max(dsp/a)+dsp2/a,(STAT2.bend.UB+STAT2.bar.US)/angles.Kf(10),'c-');
% Between cyan and magenta is the portion of energy for bending.
plot(max(dsp/a)+dsp2/a,STAT2.bar.US/angles.Kf(10),'m-');
hold off
axis([0 inf 0 inf])
xlabel('Displacement','fontsize',14);
ylabel('Stored Energy','fontsize',14);

% Kinematic path comparison: gamma_1 vs gamma_2
figure()
checkangle1 = 93; checkangle2 = 77;
alpha = alfa2/180*pi; delta = dlta/180*pi;
gamma1list = 0:0.01:2*alpha+2*delta;
gamma2list = 0:0.01:2*alpha+2*delta;
[gamma1,gamma2] = meshgrid(gamma1list,gamma2list);
flevel = -cos(alpha-delta) + (cos(alpha))^2*cos(alpha+delta) - ...
    cos(alpha+delta)*(sin(alpha))^2.*cos(gamma1).*cos(gamma2)+...
    (sin(alpha))^2.*sin(gamma1).*sin(gamma2)+...
    cos(alpha)*sin(alpha)*sin(alpha+delta).*(cos(gamma1)+cos(gamma2));
M = contour(gamma1*180/pi,gamma2*180/pi,flevel,[0,0],'color','k');
axis equal
hold on
plot(360-STAT.fold.Angle(checkangle1,:)*180/pi,STAT.fold.Angle(checkangle2,:)*180/pi)
plot(360-STAT2.fold.Angle(checkangle1,:)*180/pi,STAT2.fold.Angle(checkangle2,:)*180/pi)
xlabel('\gamma_1','fontsize',14);
ylabel('\gamma_2','fontsize',14);
```

[1] R. J. Lang, *Twists, tilings, and tessellations: Mathematical methods for geometric origami* (CRC Press, 2017).

[2] R. M. Murray, Z. Li, and S. S. Sastry, *A mathematical introduction to robotic manipulation* (CRC press, 1994).

[3] K. Liu and G. H. Paulino, Nonlinear mechanics of non-rigid origami: an efficient computational approach, Proceedings of the Royal Society A **473**, 20170348 (2017).

[4] Z. Y. Wei, Z. V. Guo, L. Dudte, H. Y. Liang, and L. Mahadevan, Geometric mechanics of periodic pleated origami, Physical Review Letters **110**, 215501 (2013).

[5] P. P. Pratapa, K. Liu, and G. H. Paulino, Geometric mechanics of origami patterns exhibiting Poisson's ratio switch by breaking mountain and valley assignment, Physical Review Letters **122**, 155501 (2019).

[6] S. Timoshenko and J. N. Goodier, *Theory of elasticity* (McGraw-Hill, New York, 1970).

[7] M. P. Do Carmo, *Differential geometry of curves and surfaces* (Courier Dover Publications, 2016).

[8] T. Ting and T. Chen, Poisson's ratio for anisotropic elastic materials can have no bounds, The Quarterly Journal of Mechanics and Applied Mathematics **58**, 73 (2005).